International Journal of Mining Science and Technology 35 (2025) 1645–1662

Contents lists available at ScienceDirect

International Journal of Mining Science and Technology

journal homepage: www.elsevier.com/locate/ijmst

A nonlinear hydraulic fracture propagation criterion considering the fracture process zone

Senlin Luo [a], Guangqing Zhang [a,b,*], Yansen Ling [a], Jinmiao Tan [c], Renyi Qiu [a], Bin Sun [a]

[a] College of Petroleum Engineering, China University of Petroleum-Beijing, Beijing 102249, China
[b] State Key Laboratory of Petroleum Resources and Prospecting, China University of Petroleum-Beijing, Beijing 102249, China
[c] College of Geosciences, China University of Petroleum-Beijing, Beijing 102249, China

ARTICLE INFO

Article history:
Received 26 May 2025
Received in revised form 12 August 2025
Accepted 18 September 2025
Available online 27 October 2025

Keywords:
Hydraulic fracturing
Fracture process zone
Nonlinear fracturing
Breakdown pressure

ABSTRACT

The linear elastic hydraulic fracture criterion is not applicable to deep reservoirs when nonlinear behavior is present over an extensive zone at the fracture tip. This study aims to develop a criterion for nonlinear hydraulic fracture considering the fracture process zone (FPZ) and seeks to reveal the causes of nonlinearity during fracture propagation in deep reservoirs. A closing stress profile considering the in-situ stress was established by using the cohesive zone model (CZM) to describe the FPZ at the fracture tip. An analytical model for the FPZ length was derived, while the criterion for nonlinear fracture propagation was proposed. The FPZ fully developed and the fracture began to propagate when the apparent stress intensity at the fracture tip reached the apparent fracture toughness or when the in-situ stress intensity reached the in-situ fracture toughness. The proposed criterion can clearly determine the length of the FPZ, accurately predict the breakdown pressure during fracturing operations, and establish a relationship between these two parameters. It addresses the inherent limitations of conventional linear elastic fracture mechanics (LEFM), which often underestimates fracture toughness and neglects the effects of the FPZ. This research is expected to enhance the fracturing design in deep reservoirs.

1. Introduction

As exploration and development technologies advance, oil and gas exploration has increasingly targeted deep reservoirs over the past few decades (>4500 m) [1–3]. Medium and deep reservoirs have contributed to 30% of the newly discovered hydrocarbon reserves. Currently, deep reservoirs account for 34.3% of global oil reserves and 59.5% of natural gas reserves. However, these reservoirs remain underexplored due to their unsatisfactory physical properties and often require hydraulic fracturing for effective industrial exploration [4–6]. In deep or ultra-deep reservoirs, the rock fracture mechanism transitions from quasi-brittle to plastic or ductile, and the nonlinear fracture process zone at the hydraulic fracture tip dominates the extension and propagation of the fracture. Conventional LEFM criteria have demonstrated limitations in addressing fracture problems within such reservoirs. The LEFM criterion assumes that the stress field at the fracture tip exhibits linear singularity but neglects the nonlinear fracture behavior at the fracture tip that arises under high-stress conditions. Consequently, fracture toughness values predicted using LEFM criteria are underestimated, resulting in an underestimation of reservoir breakdown pressures [7–10]. Given that existing LEFM criteria fail to adequately describe the nonlinear fracture behavior at the fracture tip, it is urgent to develop fracture propagation criteria that take into account nonlinear fracture behavior. This would enable a better characterization of the strengthening effect of in-situ stress on fracture toughness and provide deeper insights into the nonlinear mechanism governing fracture propagation.

The fracture process zone in hydraulic fracturing refers to the region where progressive rock damage occurs at the fracture tip, accompanied by the accumulation of numerous microcracks. This region is the primary site of energy dissipation, which is used to overcome the rock cohesive stress, generate new microcracks, and counteract friction between particles. Specifically, highly concentrated stress at the fracture tip causes natural defects within the rock, such as micropores, microcracks, and mineral grain boundaries, to act as stress concentration points. These defects ultimately lead to the formation of numerous microcracks. This process results in a significant decrease in the local stiffness and strength of the rock. The rock within the FPZ exhibits plastic rather than elastic deformation, demonstrating pronounced nonlinear stress-softening behavior [8,11,12]. The size of the FPZ and the

---

* Corresponding author.
E-mail address: zhangguangqing@cup.edu.cn (G. Zhang).

https://doi.org/10.1016/j.ijmst.2025.09.007
2095-2686/

distribution of cohesive stress significantly affect the fracture characteristics and fracture propagation. Current evidence indicates that the size of the FPZ at the fracture tip is on the order of meters, while the length of the hydraulic fracture is on the order of hundreds of meters, i.e., $r/a \approx 0.01 \ll 1$ [10]. The r represent the characteristic size of the nonlinear region, a represent the characteristic size of the hydraulic fracture, and the ratio r/a represent the relative length of the nonlinear region. This indicates that the hydraulic fracture tip zone conforms to a small-scale yielding condition. In this case, most of the zone remains in the elastic regime, and linear elastic fracture theory can still be applied in engineering contexts. Stress intensity, or its appropriate corrected form, can still characterize the strength of the stress field near the fracture tip.

Currently, fracture tests under atmospheric pressure underestimate the fracture stress intensity, leading to inaccurate fracture criteria under in-situ stress states [13–16]. As shown in Fig. 1, fracture toughness may increase by 10% to 480% under confining pressure [10,17]. Therefore, hydraulic fracture analysis must account for both the intrinsic properties of rock materials and in-situ stress, as these rocks are deeply buried and subjected to high confining pressure. Rubin [18] proposed the concept of apparent fracture toughness while investigating dike propagation under high confining pressure. Apparent fracture toughness is broadly defined as the rock's resistance to fracture propagation under multifactorial influences, including intrinsic material properties, in-situ stress, temperature, and loading conditions, and other factors. Numerous experiments have demonstrated that the apparent fracture toughness increases with confining pressure [17,19–22]. Additionally, field fracturing results indicate that the apparent fracture toughness is enhanced by both in-situ stress and fracture length [10,23]. Field tests of hydraulic fracturing show that the injection pressure obtained via constant fracture toughness is lower than the measured pressure [23,24]. Scholz [25] speculated a square-root dependence of apparent fracture toughness on fracture length. Yue et al. [9] developed an analytical model for FPZ and fluid lag length and demonstrated that apparent toughness was increased by both confining pressure and fluid lag length. Compressive stresses within the FPZ and fluid lag zone prevent fracture opening. Consequently, higher in-situ stress necessitates greater fluid pressure to sustain fracture propagation. While these studies focus on the rock's ability to resist fracturing based on intrinsic rock properties and in-situ stress, research has also demonstrated that in-situ stress enhances the intrinsic fracture properties of rocks, specifically in-situ fracture toughness [19,26]. Zhao and Roegiers [26] derived an in-situ fracture toughness equation using the Dugdale model and superposition principle. They indicated that the in-situ fracture toughness is related to the in-situ stress, tensile strength, and solution method. Luo et al. [19] established a three-point bending model under confining pressure via discrete elements and revealed that the actual fracture toughness first increased linearly with confining pressure before stabilizing. While previous studies have clarified the nonlinear behavior of the fracture tip and the effect of confining pressure on rock fracture toughness, the nonlinear mechanism by which the FPZ affects fracture toughness have not yet been thoroughly explored.

Furthermore, some researchers have initially established the hydraulic fracture criteria considering the nonlinear region, which can describe the development phenomenon of FPZ. Assuming that microcracks are caused by tensile stress and that the size of the microcrack zone is determined by the tensile strength, Schmidt [27] proposed a microcrack model to describe the tensile state at the hydraulic fracture tip. This model assumes constant fracture toughness under confining pressure, with the dimensions of the microcrack zone inversely proportional to hydrostatic confining pressure. Sato and Hashida [28] provided analytical solutions for apparent fracture toughness and FPZ size based on the cohesive zone model. Their models defined apparent fracture toughness as a function of tensile strength and confining pressure, while FPZ length diminished under higher confining pressure. Based on a hydraulic fracture model that incorporates a cohesive zone at the

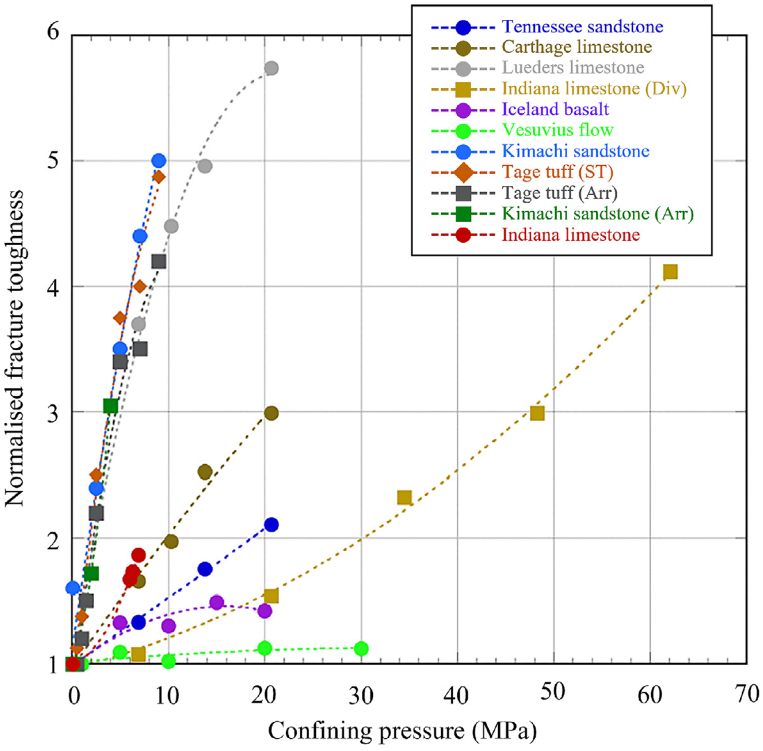

Fig. 1. Influence of confining pressure on normalized fracture toughness of the rock [10,17].

fracture tip using the Barenblatt's method, Mokryakov [29] derived the limiting form of the cohesive zone and evaluated the limited fracture toughness. Zhao and Roegiers [26] formulated an FPZ analytical solution using a penny-shaped crack model. They indicated that the FPZ length is dependent on breakdown pressure, shut-in pressure, rock tensile strength, in-situ stress, and fracture length. Although research has increasingly focused on the influence of FPZ on fracture propagation, most studies still assume fracture toughness to be constant and fail to fully account for the influence of in-situ stress on rock fracture performance. In addition, existing models inadequately elucidate the development of the FPZ and lack robust experimental validation.

In this study, we derived a nonlinear hydraulic fracture criterion that considers the FPZ. Within the LEFM framework, the CZM was adopted to describe the FPZ at the fracture tip. A closing stress distribution profile for the FPZ was formulated by incorporating uniformly distributed in-situ stress into the cohesive stress profile. This study derived three key parameters by assuming zero stress intensity at the fracture tip: apparent fracture toughness, in-situ fracture toughness, and FPZ length. Additionally, the correlation between breakdown pressure and FPZ length was developed, and a nonlinear hydraulic fracture propagation criterion considering FPZ was established. The reliability of the proposed criterion was validated through a visualized hydraulic fracturing experiment and a true triaxial hydraulic fracturing experiment. The novel nonlinear hydraulic fracture propagation criterion proposed in this study provides theoretical guidance for predicting nonlinear fracture behavior in deep reservoirs.

2. Derivation of nonlinear hydraulic fracture propagation criterion

2.1. Problem description

The conventional linear elastic hydraulic fracture criterion fails to account for the FPZ, and the stress intensity factor at the fracture tip can be expressed as follows:

$$K_{\mathrm{I}} = P_{\mathrm{f}}\sqrt{R_0}(h_0+h_a) - \sigma_{\mathrm{H}}\sqrt{R_0}f(b) - \sigma_{\mathrm{h}}\sqrt{R_0}g(b) \tag{1}$$

where P_{f} is the fluid pressure, MPa; R_0 the wellbore radius, mm; h_0, h_a, $f(b)$, and $g(b)$ the dimensionless stress intensity functions; and σ_{H} and σ_{h} the maximum and minimum horizontal in-situ stresses, respectively, MPa.

Fracture propagation initiates when the stress intensity factor at the fracture tip reaches the fracture toughness of the rock, which is represented by the condition $K_{\mathrm{I}} = K_{\mathrm{IC}}$. At this point, the fluid pressure is expressed as:

$$P_{\mathrm{b}} = \frac{1}{h_0+h_a}\left(\frac{K_{\mathrm{IC}}}{\sqrt{R_0}} + \sigma_{\mathrm{H}}f(b) + \sigma_{\mathrm{h}}g(b)\right) \tag{2}$$

where P_{b} is the breakdown pressure, MPa; K_{IC} is the fracture toughness, MPa·mm$^{0.5}$.

Furthermore, we considered the FPZ at the hydraulic fracture tip by employing the CZM, which effectively describes the development mechanism and nonlinear fracture propagation of FPZ [30,31]. The foundational work on CZM can be traced back to Dugdale and Barenblatt in the 1960s [11,32]. The purpose of the CZM is to mitigate fracture tip stress singularity typically found at the fracture tip in linear elastic fracture mechanics [11,33]. When a fracture opens, both strain and stress singularities arise at its tip; however, the physical stress at the fracture tip cannot be infinitely large. Dugdale experimentally identified a band-shaped yield zone at the fracture tip. Barenblatt proposed that cohesive stress, which is related to the fracture opening displacement, exists at the fracture tip. He posited that the combined stress intensity factor arising from cohesive stress and external load is zero, thereby eliminating the singularity at the tip [11,32,33]. Fig. 2 illustrates the two-dimensional stress state of the hydraulic fracture. It is assumed that the hydraulic fracture is straight and symmetrical (mode I fracture), and the fluid lag at the fracture tip is not considered. The cohesive stress σ is distributed throughout the FPZ, which has a length of r_{p}. The total fracture length is $2c$, with the free fracture length being $2a$. The free fracture surface is subjected to fluid pressure P_{f}, and there is no fluid in the FPZ. The effects of maximum horizontal in-situ stress and vertical in-situ stress are excluded, and the fracture is constrained by the far-field minimum horizontal in-situ stress. The compressive stress is defined as positive in the subsequent analysis.

To simplify the model's stress state, the original problem is decomposed into two sub-problems. As depicted in Fig. 3, the first sub-state involves an applied stress ΔP ($\Delta P = -P_{\mathrm{f}} + \sigma_{\mathrm{h}}$) acting on the free fracture to induce fracture opening. The second sub-state involves a closing stress σ^{close} ($\sigma^{\mathrm{close}} = \sigma + \sigma_{\mathrm{h}}$) in the FPZ to resist fracture opening. Since the singular behavior of stress no longer exists at the hydraulic fracture tip, the total stress intensity factor is zero:

$$K_{\mathrm{I}} = K_{\mathrm{I}}^{\mathrm{load}} + K_{\mathrm{I}}^{\mathrm{close}} = 0 \tag{3}$$

where K_{I} is the total stress intensity factor at fracture tip, MPa·mm$^{0.5}$; $K_{\mathrm{I}}^{\mathrm{load}}$ the stress intensity factor caused by applied stress, MPa·mm$^{0.5}$; and $K_{\mathrm{I}}^{\mathrm{close}}$ the stress intensity factor induced by the closing stress, MPa·mm$^{0.5}$. Subsequently, based on this regulation, the apparent fracture toughness, in-situ fracture toughness, FPZ length, breakdown pressure, and the relationship between FPZ length and breakdown pressure were derived.

2.2. Apparent fracture toughness

This study defines apparent fracture toughness ($K_{\mathrm{IC}}^{\mathrm{close}}$) to measure the rock's resistance to fracture propagation under in-situ stress and confining pressure. There are two methods to calculate $K_{\mathrm{IC}}^{\mathrm{close}}$. The first method involves calculating $K_{\mathrm{IC}}^{\mathrm{load}}$ through Eq. (3) to indirectly obtain $K_{\mathrm{IC}}^{\mathrm{close}}$, while the second method directly derives $K_{\mathrm{IC}}^{\mathrm{close}}$ though integration of the closing stress.

In the first method, since the FPZ size is much smaller than that of the free fracture, the stress intensity factor caused by the applied stress remains within the category of the LEFM [34]. The corresponding calculation equation is given as follows:

$$K_{\mathrm{I}}^{\mathrm{load}} = (-P_{\mathrm{f}} + \sigma_{\mathrm{h}})\sqrt{\pi\left(a + r_{\mathrm{p}}\right)} \tag{4}$$

Based on Taylor expansion, Eq. (4) can be transformed into:

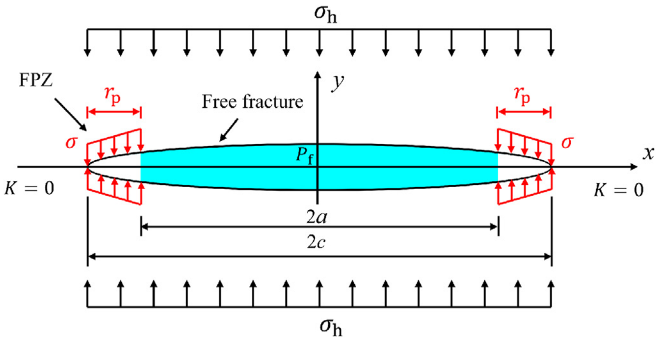

Fig. 2. Schematic diagram of hydraulic fracture.

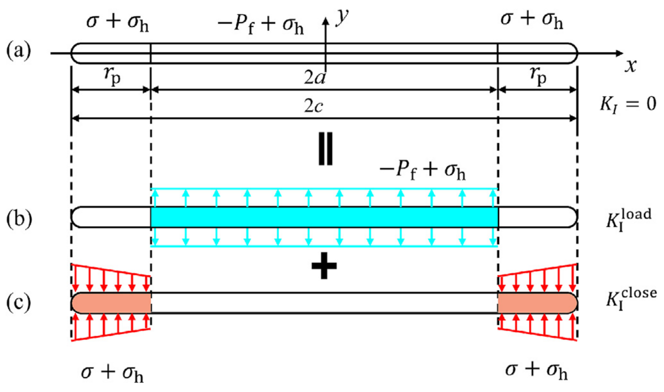

Fig. 3. The original problem is decomposed into two sub-problems using the superposition method: (a) Original problem: original stress state; (b) First sub-problem: applied stress state; and (c) Second sub-problem: closing stress state.

$$K_{\mathrm{I}}^{\mathrm{load}}=(-P_{\mathrm{f}}+\sigma_{\mathrm{h}})\sqrt{\pi a}\left(1+\tfrac{r_{\mathrm{p}}}{2a}+o(r_{\mathrm{p}})\right) \tag{5}$$

Further, when $r_{\mathrm{p}}/a \ll 1$, Eq. (5) can be simplified as:

$$K_{\mathrm{I}}^{\mathrm{load}}=(-P_{\mathrm{f}}+\sigma_{\mathrm{h}})\sqrt{\pi a} \tag{6}$$

According to Eq. (3), the stress intensity factor $K_{\mathrm{I}}^{\mathrm{close}}$ induced by the closing stress can be indirectly determined. This is referred to as the apparent stress intensity factor (Apparent SIF):

$$K_{\mathrm{I}}^{\mathrm{close}}=(P_{\mathrm{f}}-\sigma_{\mathrm{h}})\sqrt{\pi a} \tag{7}$$

where $P_{\mathrm{f}}-\sigma_{\mathrm{h}}$ is also referred to as the net pressure, MPa.

In the second method, we first describe the expression for the closing stress. As discussed in Section 2.1, the closing stress σ^{close} is composed of the cohesive stress σ distributed through the FPZ and the uniformly distributed far-field stress. Therefore, the following relation can be obtained.

$$\sigma^{\mathrm{close}}=\sigma+\sigma_{\mathrm{h}} \tag{8}$$

According to the CZM, the cohesive stress at the tip of the FPZ reaches the maximum value, which corresponds to the material's tensile strength f_{t}, and diminishes to zero at the end of the FPZ. The cohesive stress σ follows the general distribution:

$$\sigma(\xi)=f_{\mathrm{t}}F(\xi) \tag{9}$$

where $\xi=r/r_{\mathrm{p}}$ is the dimensionless distance from the tip of the FPZ to the free fracture tip, with $0<\xi<1$; and $F(\xi)$ a dimensionless function describing the cohesive stress distribution in the FPZ. A common cohesive stress distribution function is as follows:

$$F(\xi)=(1-\xi)^n, n\in R \tag{10}$$

Overall, the general expression for the closing stress σ^{close} in the FPZ is:

$$\sigma^{\mathrm{close}}=\sigma_{\mathrm{h}}+f_{\mathrm{t}}F(\xi) \tag{11}$$

Assuming that the cohesive stress under in-situ stress follows a linear distribution ($n=1$), as shown in Fig. 4a, the expression for the closing stress in the FPZ is:

$$\sigma^{\mathrm{close}}=\sigma_{\mathrm{h}}+(1-\xi)f_{\mathrm{t}} \tag{12}$$

We consider a central crack with a length of 2a in an infinite plate, which is subjected to a symmetrical point load per unit thickness, as shown in Fig. 5. The stress intensity factor $K_{\mathrm{I}}^{\mathrm{P}}$ is given as follows [35]:

$$K_{\mathrm{I}}^{\mathrm{P}}=\tfrac{P}{\sqrt{\pi a}}\sqrt{\tfrac{a+x}{a-x}} \tag{13}$$

Let $a-x=r$, when the FPZ size is much smaller than the free fracture size, i.e., $r<r_{\mathrm{p}}\ll a$, so $a+x=2a-r\approx 2a$, and $\sqrt{(a+x)/(a-x)}=\sqrt{2a/r}$. Substituting this formula into Eq. (13) yields [36]:

$$K_{\mathrm{I}}^{\mathrm{P}}\approx\tfrac{P}{\sqrt{\pi a}}\sqrt{\tfrac{2a}{r}}=P\sqrt{\tfrac{2}{\pi r}} \tag{14}$$

Based on Eq. (14) and the superposition principle, the apparent stress intensity factor $K_{\mathrm{I}}^{\mathrm{close}}$, induced by the closing stress σ^{close}, is obtained from the following equation:

$$K_{\mathrm{I}}^{\mathrm{close}}=\int_0^{r_{\mathrm{p}}}\sqrt{\tfrac{2}{\pi r}}\sigma^{\mathrm{close}}dr \tag{15}$$

where $\mathrm{d}P=\sigma^{\mathrm{close}}\mathrm{d}r$. Since $\sigma^{\mathrm{close}}=\sigma_{\mathrm{h}}+(1-\xi)f_{\mathrm{t}}$, $\xi=r/r_{\mathrm{p}}$, and $\mathrm{d}r=r_{\mathrm{p}}\mathrm{d}\xi$, Eq. (15) can be reformulated as:

$$K_{\mathrm{I}}^{\mathrm{close}}=\sqrt{\tfrac{2r_{\mathrm{p}}}{\pi}}\int_0^1\tfrac{\sigma_{\mathrm{h}}+(1-\xi)f_{\mathrm{t}}}{\sqrt{\xi}}d\xi \tag{16}$$

Integrating Eq. (16) yields the analytical expression of $K_{\mathrm{I}}^{\mathrm{close}}$ as follows:

$$K_{\mathrm{I}}^{\mathrm{close}}=\left(\sigma_{\mathrm{h}}+\tfrac{2}{3}f_{\mathrm{t}}\right)\sqrt{\tfrac{8r_{\mathrm{p}}}{\pi}} \tag{17}$$

In summary, the analytical expression for the $K_{\mathrm{I}}^{\mathrm{close}}$ is as follows:

$$K_{\mathrm{I}}^{\mathrm{close}}=\begin{cases}(P_{\mathrm{f}}-\sigma_{\mathrm{h}})\sqrt{\pi a}\\ \left(\sigma_{\mathrm{h}}+\tfrac{2}{3}f_{\mathrm{t}}\right)\sqrt{\tfrac{8r_{\mathrm{p}}}{\pi}}\end{cases} \tag{18}$$

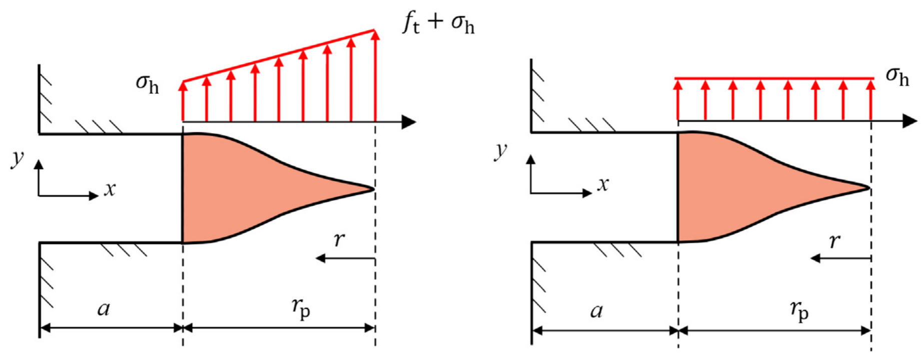

(a) The closing stress profile

(b) In-situ stress profile

Fig. 4. Stress distribution in the FPZ.

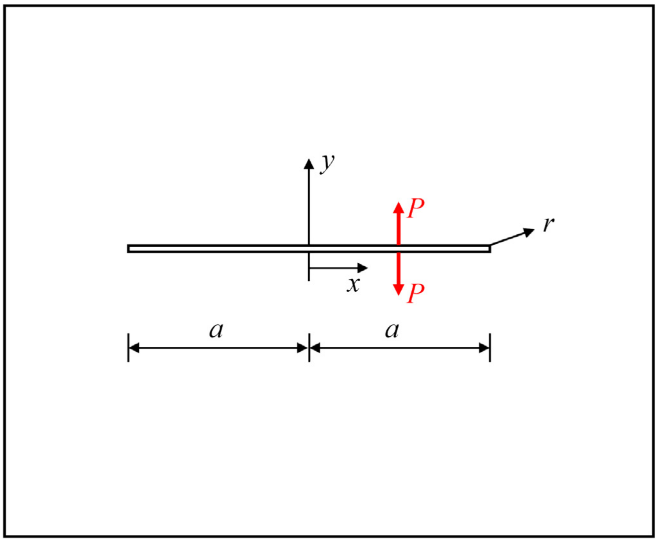

Fig. 5. Central fracture of an infinite plate under point load per unit thickness.

The apparent fracture toughness can be obtained when the fluid pressure reaches its peak ($P_f = P_b$) or when the FPZ is fully developed ($r_p = r_{pmax}$).

2.3. In-situ fracture toughness

In-situ fracture toughness K_{IC}^{i} refers to the intrinsic fracture characteristics of rock, which is determined by residual cohesive stress σ' distributed within the FPZ after the removal of in-situ stress. Theoretically, K_{IC}^{i} can be derived by integrating the residual cohesive stress. However, the cohesive stress distribution in the FPZ is affected by the in-situ stress, and the functional relationship between $\sigma' = f(\sigma_h)$ has remained unquantified in previous studies. Consequently, it is challenging to derive the in-situ fracture toughness K_{IC}^{i} through the residual cohesive stress σ'.

To address computational limitations arising from the ambiguous distribution of residual cohesive stress σ', the closing stress state is decomposed into a residual stress state and an in-situ stress state using the superposition method. Zhao and Roegiers [26] verified the reliability of this method in 1993, which is expressed as follows:

$$K_I^{close} = K_I^{i} + K_I^{h} \tag{19}$$

where K_I^{i} is the in-situ stress intensity factor induced by the residual cohesive stress, MPa·mm$^{0.5}$; and K_I^{h} the stress intensity factor induced by the in-situ stress, MPa·mm$^{0.5}$. Therefore, the in-situ stress intensity factor K_I^{i} can be obtained by subtracting the stress intensity factor K_I^{h} induced by the in-situ stress from the apparent stress intensity factor K_I^{close}. The in-situ stress σ_h is a known uniformly distributed stress, as illustrated in Fig. 3b. The expression for K_I^{h} is derived using the integration method outlined in Section 2.2:

$$K_I^{h} = \sigma_h\sqrt{\frac{8r_p}{\pi}} \tag{20}$$

Substituting Eq. (17) into Eq. (20) yields the relationship between K_I^{h} and K_I^{close}:

$$K_I^{h} = \frac{3\sigma_h}{3\sigma_h+2f_t}K_I^{close} \tag{21}$$

Further substituting Eq. (21) into Eq. (19) yields the relationship between K_I^{i} and K_I^{close}:

$$K_I^{i} = \left(1-\frac{3\sigma_h}{3\sigma_h+2f_t}\right)K_I^{close} \tag{22}$$

Substituting Eq. (7) into Eq. (22) yields the first analytic expression for the in-situ stress intensity factor K_I^{i}:

$$K_I^{i} = \left(1-\frac{3\sigma_h}{3\sigma_h+2f_t}\right)(P_f-\sigma_h)\sqrt{\pi a} \tag{23}$$

Substituting Eq. (17) into Eq. (22) yields the second analytic expression for the in-situ stress intensity factor K_I^{i}:

$$K_I^{i} = \frac{2f_t}{3}\sqrt{\frac{8r_p}{\pi}} \tag{24}$$

In summary, the analytical expression for K_I^{i} is as follows:

$$K_I^{i} = \begin{cases} \left(1-\frac{3\sigma_h}{3\sigma_h+2f_t}\right)(P_f-\sigma_h)\sqrt{\pi a} \\ \frac{2f_t}{3}\sqrt{\frac{8r_p}{\pi}} \end{cases} \tag{25}$$

The in-situ fracture toughness can be determined when the fluid pressure reaches its peak ($P_f = P_b$) or when the FPZ is fully developed ($r_p = r_{pmax}$).

2.4. The influence of in-situ stress on apparent and in-situ fracture toughness

To reveal the influence of in-situ stress on both apparent and in-situ fracture toughness, a virtual fracturing model was constructed using the parameter values listed in Table 1 as the initial inputs. The minimum horizontal stress was varied between 20 and 100 MPa, with an interval of 10 MPa, while the horizontal stress difference was set at 10 MPa. Previous studies have demonstrated that in-situ stress exerts a strengthening effect on the tensile strength of rock. In this study, it is assumed that the tensile strength equals the sum of the minimum in-situ stress and the unconfined strength, where the unconfined strength was set at 2 MPa. The breakdown pressure of the reservoir was calculated based on the minimum horizontal stress, maximum horizontal stress, and tensile strength. Substituting the parameter values from Table 1 into Eqs. (18) and (25) allowed for the determination of both apparent and in-situ fracture toughness.

Fig. 6 illustrated that the apparent fracture toughness exhibited a linear relationship with the minimum horizontal stress and was found to be 2–3 orders of magnitude higher than values measured in laboratory experiments. The in-situ fracture toughness was found to be $1-3\sigma_h/(3\sigma_h+2f_t)$ times the apparent fracture toughness. Furthermore, higher minimum horizontal stress led to a lower multiple, indicating that more energy is consumed to overcome the in-situ stress in deep or ultra-deep reservoirs.

2.5. Nonlinear hydraulic fracture propagation criterion

The nonlinear fracture process zone at the fracture tip governs fracture propagation and extension during hydraulic fracturing in deep reservoirs. Therefore, this study established a nonlinear hydraulic fracture propagation criterion that explicitly accounts for the FPZ. The primary objectives of this criterion are to determine the size of the nonlinear FPZ, predict the breakdown pressure during fracturing operations, and establish a quantitative relationship between these two parameters. Ultimately, this criterion was applied to the design of fracturing operation strategies for deep or ultra-deep reservoirs.

Table 1
The basic parameters of the virtual fracturing model.

a (mm)	σ_h (MPa)	σ_H (MPa)	f_t (MPa)	P_b (MPa)
500	20~100	$\sigma_H = \sigma_h + 10$	$f_t = \sigma_h + 2.0$	$P_b = 3\sigma_h - \sigma_H + f_t$

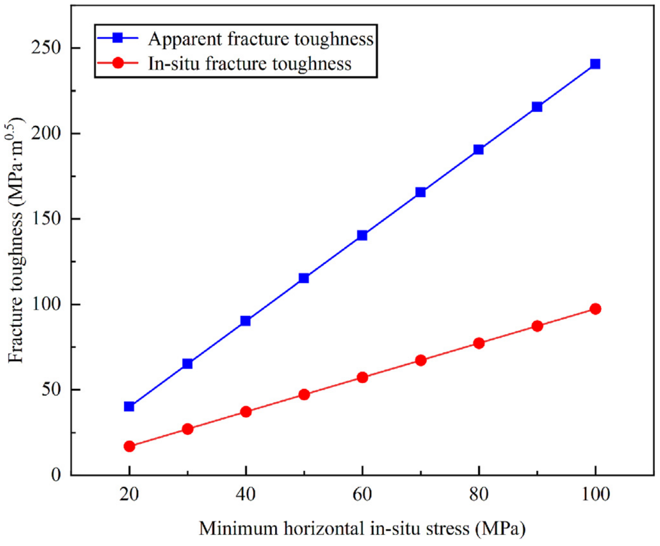

Fig. 6. The relationship between fracture toughness and minimum in-situ stress.

Firstly, we analyze the relationship between r_p and K_I^i and K_I^{close}. The transformation of Eq. (17) yields the formulation for r_p as a function of K_I^{close}:

$$r_p = \frac{9\pi}{8}\left(\frac{K_I^{close}}{3\sigma_h+2f_t}\right)^2 \tag{26}$$

Similarly, the formulation for r_p as a function of K_I^i is obtained by transforming Eq. (24):

$$r_p = \frac{9\pi}{32}\left(\frac{K_I^i}{f_t}\right)^2 \tag{27}$$

In contrast to the traditional linear elastic hydraulic fracture propagation criterion, this study quantitatively measured the relationship between fluid pressure, apparent SIF, in-situ SIF, and FPZ length. The FPZ length was determined to be a quadratic function of both the apparent SIF and the in-situ SIF. As the SIF increased, the FPZ length increased in a parabolic manner. Furthermore, a higher SIF resulted in a greater stress concentration effect at the fracture tip, which in turn caused a larger area to transition into the plastic deformation state, thereby leading to a larger FPZ range. In practical hydraulic fracturing operations, a thorough analysis of the relationship between SIF and FPZ can enhance the predictability of fracture propagation behavior and the fracture performance of reservoir rocks.

Subsequently, we analyzed the relationship between FPZ length r_p and fluid pressure P_f. The FPZ length was calculated based on the condition that the total stress intensity factor at the fracture tip equals zero. This relationship can be derived though an analysis of either the two formulations for the apparent SIF or the two formulations for the in-situ SIF, which is called the correlation equation:

$$r_p = \frac{9a\pi^2}{8}\left(\frac{P_f-\sigma_h}{3\sigma_h+2f_t}\right)^2 \tag{28}$$

The length of FPZ is affected by two engineering factors (a, P_f) and geological factors (σ_h, f_t). For a specific reservoir, the FPZ length is mainly dominated by fluid pressure and fracture length when the in-situ stress and rock tensile strength are determined. Notably, the FPZ length is a quadratic function of the injected fluid pressure.

When the apparent stress intensity factor at the fracture tip reaches the apparent fracture toughness ($K_I^{close} = K_{IC}^{close}$) or when the in-situ stress intensity factor reaches the in-situ fracture toughness ($K_I^i = K_{IC}^i$), the FPZ is fully developed ($r_p = r_{pmax}$), at which point the fracture begins to propagate. This phenomenon is referred to as the nonlinear hydraulic fracture propagation criterion. From this analysis, we can derive the breakdown pressure P_b at which the fracture propagates unstably:

$$P_b = \begin{cases} \frac{K_{IC}^{close}}{\sqrt{\pi a}} + \sigma_h \\ \left(1+\frac{3\sigma_h}{2f_t}\right)\frac{1}{\sqrt{\pi a}}K_{IC}^i + \sigma_h \\ \frac{2}{3\pi}(3\sigma_h+2f_t)\sqrt{\frac{2r_{pmax}}{a}} + \sigma_h \end{cases} \tag{29}$$

The analysis of the influence of in-situ stress on both apparent fracture toughness and in-situ fracture toughness presented in Section 2.4 was performed under the condition of a known breakdown pressure. However, practical fracturing design requires predicting the breakdown pressure based on known apparent fracture toughness, in-situ fracture toughness, and tensile strength. Therefore, these parameters must be obtained through fracture experiments under confining pressure conditions. This approach ensures that the reservoir's fracture performance is accurately represented under in-situ stress conditions.

The specific application process of the nonlinear hydraulic fracture propagation criterion is illustrated in Fig. 7. Step 1: Perform a three-point bending test or a Brazilian test under minimum horizontal in-situ stress conditions. Step 2: Calculate the apparent fracture toughness, in-situ fracture toughness, and tensile strength using the experimental data. Step 3: Apply the proposed analytical model to predict both the FPZ length and breakdown pressure. The visual hydraulic fracturing experiments described in Section 3 were conducted to validate the correlation equation (FPZ length), while the true triaxial hydraulic fracturing experiments detailed in Section 4 were performed to verify the breakdown pressure and to analyze the dynamic evolution of the FPZ.

3. Verification of correlation equation based on visual fracturing experiment

3.1. Visual hydraulic fracturing experiments

3.1.1. Experimental specimen

To minimize the influence of additional factors, such as rock defects, on the experimental results, structurally uniform yellow sandstone specimens sourced from Sichuan, China, were utilized in this study. The sandstone matrix exhibits a predominant particle size distribution ranging from 0.25 to 0.50 mm. The mineralogical composition comprises dominant albite (66.2%), quartz (21.7%), and minor clay minerals. The mechanical properties of the specimens include a tensile strength of 1.4 MPa, a uniaxial com-

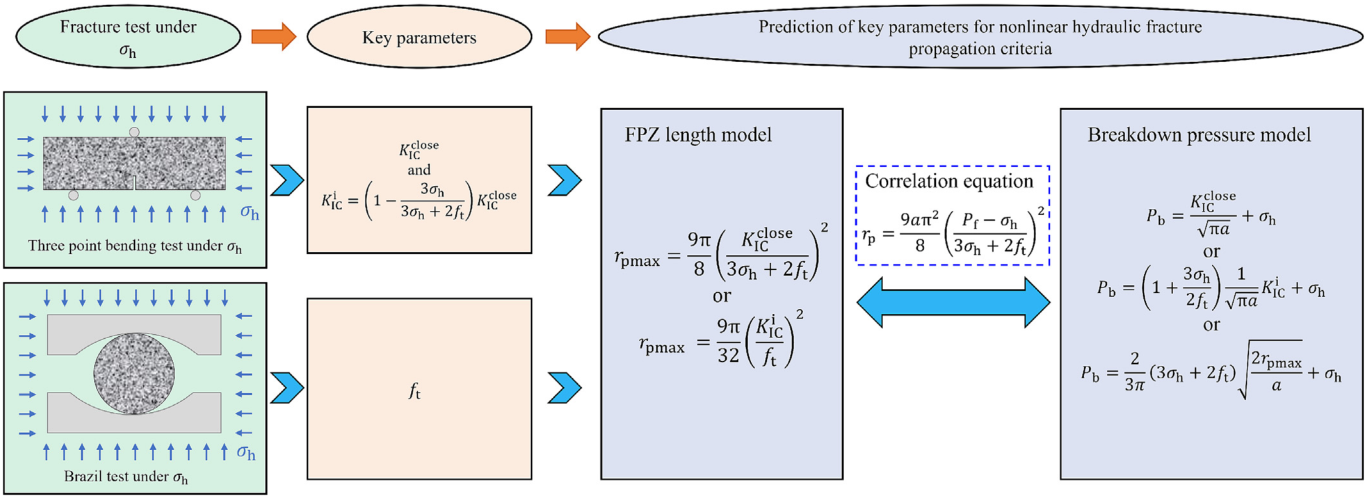

Fig. 7. The application process of the nonlinear hydraulic fracture propagation criterion.

pressive strength of 12.7 MPa, an elastic modulus of 2.5 GPa, and a Poisson's ratio of 0.36.

The specimen was fabricated into a rock plate measuring 200 mm × 200 mm × 50 mm, and a 20 mm-diameter circular hole was drilled at its geometric center to replicate the injection wellbore, as shown in Fig. 8c. To simulate the perforation section relevant to hydraulic fracturing, prefabricated cracks with a length of 10 mm were created on both sides of the wellbore using rock wire-cutting technology. Prior to experimentation, the specimens were oven-dried at 85 °C for 48 h to remove pore moisture and eliminate its potential effects on fracture behavior.

3.1.2. Experimental equipment

The experimental setup utilized a visual hydraulic fracturing test device (Fig. 8), designed by the China University of Petroleum (Beijing), to monitor the development of the FPZ and the fracture propagation. This device consists of three-axis hydraulic jacks for the application of triaxial stress, a light source, a high-resolution camera, a constant-flow-rate injection pump, pressure monitors, and other ancillary equipment. A transparent acrylic plate is integrated above the device to facilitate recording of the fracture propagation process. The injection borehole is epoxy-sealed at both its upper and lower extremities, while a 30 mm central interval was retained for the installation of fracturing fluid injection pipe. To prevent mechanical interference between the specimen and acrylic interface, a soft transparent tape was applied to the rock surface. Jacks provide horizontal and vertical stress in three directions. As shown in Fig. 8, the minimum in-situ stress was applied in the *x*-direction, which is perpendicular to the prefabricated crack, to facilitate the fracture propagation along the prefabricated crack.

During the experiments, fracturing fluid was injected at a constant rate of 10 mL/min. The fracturing fluid comprised water, guar gum (1 wt%), and a red tracer dye, yielding a final viscosity of 300 cP. To induce vertical fracture propagation for optical monitoring, the triaxial stresses were configured as follows: vertical stress (σ_V) is 6 MPa (maximum); *x*-direction stress (σ_h) is 1 MPa (minimum); and *y*-direction stress (σ_H) is 3 MPa (intermediate).

3.1.3. DIC monitoring method

The development of the FPZ was monitored via digital image correlation (DIC), a non-contact optical technique widely

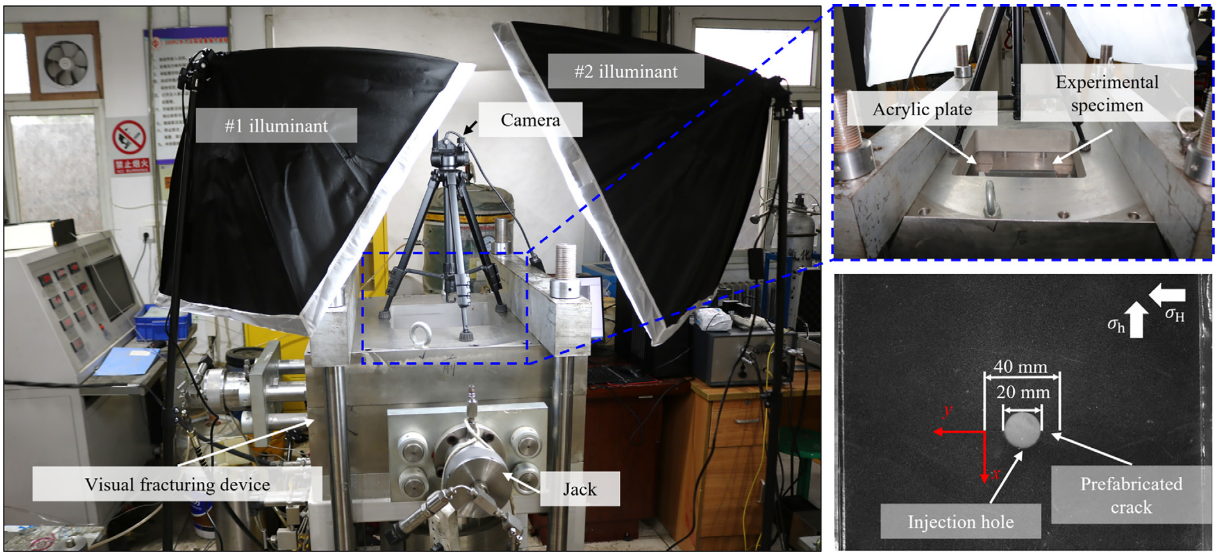

Fig. 8. The visual hydraulic fracturing test device.

employed for material deformation analysis [37,38]. In DIC, the specimen surface image is partitioned into discrete subsets, and displacement vectors are computed via cross-correlation algorithms that compare subset positions in the reference and deformed states. During the experiment, a uniform black and white speckle pattern was sprayed on the specimen surface to identify clear image subsets. A first-order shape function was introduced to describe the changes in the center position and shape of the subset:

$$x_i' = x_i + u + \frac{\partial u}{\partial x}\Delta x + \frac{\partial u}{\partial y}\Delta y \tag{30}$$

$$y_i' = y_i + v + \frac{\partial v}{\partial x}\Delta x + \frac{\partial v}{\partial y}\Delta y \tag{31}$$

where (x_i, y_i) is an arbitrary point in the reference image subset, mm; (x_i', y_i') the deformed point, mm; u and v the displacements in the x and y directions, respectively, mm; and Δx and Δy the distances from the point to the center of the image subset, mm.

After obtaining the displacement field information, the Green-Lagrangian strain field is established using the four displacement gradients:

$$\varepsilon_{xx} = \frac{1}{2}\left(2\frac{\partial u}{\partial x} + \left(\frac{\partial u}{\partial x}\right)^2 + \left(\frac{\partial v}{\partial x}\right)^2\right) \tag{32}$$

$$\varepsilon_{xy} = \frac{1}{2}\left(\frac{\partial u}{\partial y} + \frac{\partial v}{\partial x} + \frac{\partial u}{\partial x}\frac{\partial u}{\partial y} + \frac{\partial v}{\partial x}\frac{\partial v}{\partial y}\right) \tag{33}$$

$$\varepsilon_{yy} = \frac{1}{2}\left(2\frac{\partial v}{\partial y} + \left(\frac{\partial u}{\partial y}\right)^2 + \left(\frac{\partial v}{\partial y}\right)^2\right) \tag{34}$$

where ε_{xx} and ε_{yy} are strains in the x and y directions respectively, %; and ε_{xy} the shear strain, %.

3.2. Identification of FPZ initiation point and length

The injection curve and the post-experimental specimen are shown in Fig. 9. Due to the constrained dimensions of the specimens, the fracture rapidly propagated to the boundary upon reaching the peak injection pressure. As a result, stable fracture propagation after the peak could not be observed. Beyond point c (Fig. 9), the fracture extended beyond the observational field of view. As shown in Fig. 9b and c, the hydraulic fracture initiated along the prefabricated crack and propagated bilaterally until the left tip breached the boundary. Subsequent analysis focused on the left fracture. To analyze the entire process of FPZ development, it is necessary to identify the moment at which the pre-peak FPZ begins to develop. Previous research [39,40] demonstrated that FPZ initiation point coincides with the onset of nonlinearity in the injection curve. In Fig. 9a, the blue curve represents the slope dP/dt of the injection pressure curve. It was observed found that point a (t=20 s) drops significantly, which indicated the onset of FPZ development. In addition, the surface displacement characteristics of the specimen monitored by DIC can also be utilized to identify the initiation point of the FPZ.

FPZ identification has historically posed a significant challenge. However, advancements in DIC technology have led to the development of more accurate methods for identifying the FPZ tip, including displacement threshold method, strain threshold method, and displacement gradient threshold method [41–43]. In this study, we adopted the fracture opening displacement pattern proposed by Lin et al. [41,42] to identify the FPZ length. This pattern divides the rock into three regions according to the characteristics of the displacement curve and displacement gradient: the elastic zone, the FPZ, and the free fracture, as illustrated in Fig. 10a. The position at y=34.08 mm marks the elastic zone, where the displacement curve is a linear with a constant displacement gradient $\partial u/\partial x$, as shown in Fig. 10b. The position at y=23.24 mm corresponds to the FPZ, where the displacement gradient $\partial u/\partial x>0$ is significant, and it is larger in the middle and smaller on both sides. The position at y=9.29 mm indicates the hydraulic fracture. The presence of fluid pressure compressed the rocks on both sides of the fracture. This leads to a displacement gradient on both sides of the displacement curve that exhibits the characteristic of $\partial u/\partial x<0$. The hydraulic fracture tip (i.e., FPZ end) is located at y=18.90 mm, where the displacement gradients on either side of the curve show the characteristic of $\partial u/\partial x\approx 0$, which indicates that the hydraulic fracture tip is neither compressed by the fluid nor subjected to stretching within the FPZ. The FPZ tip is identified at y=28.80 mm, and its displacement curve and displacement gradient characteristics are positioned between the elastic zone and the FPZ.

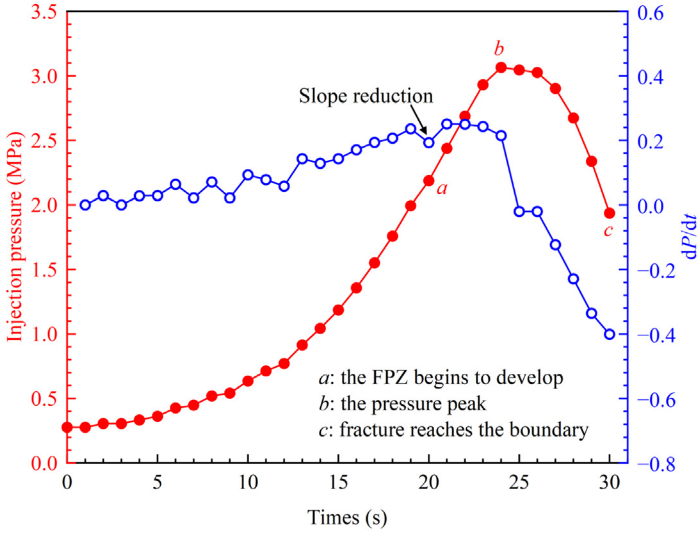

(a) Injection curve

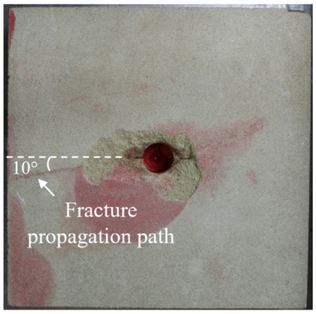

(b) Fracture morphology

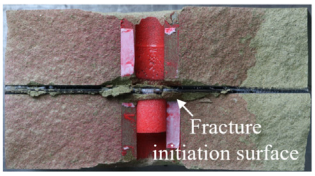

(c) Fracture cross-section

Fig. 9. Injection curve and post-experimental specimen.

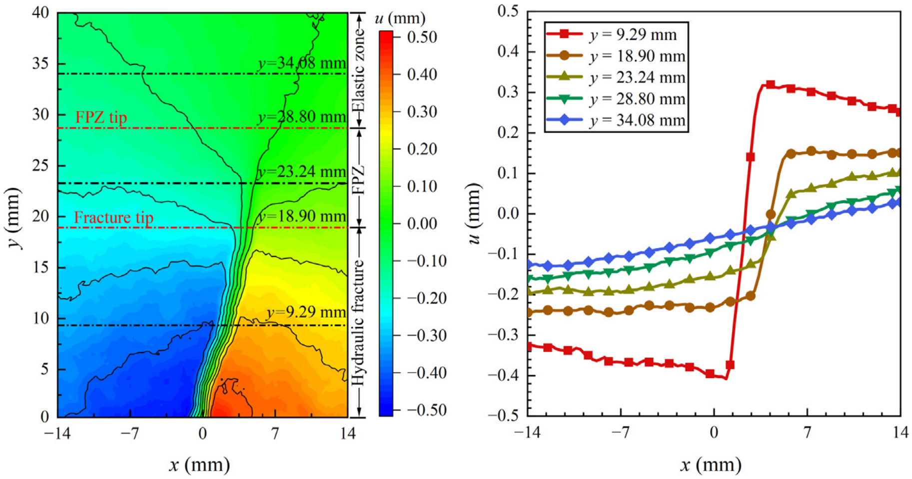

(a) Displacement nephogram (b) Displacement curve

Fig. 10. Displacement nephogram and displacement curve of the specimen at 26 s.

3.3. Analysis of fracturing process

Significant changes occurred in the displacement and strain fields on the specimen surface before and after fracture initiation. Fig. 11 shows the y-direction displacement field on the sample surface, while Fig. 12 depicts the y-direction strain field. As an elastoplastic solid material, rock underwent obvious elastoplastic deformation around the wellbore when subjected to the circumferential pressure. Fig. 11 illustrated that as fracturing fluid was continuously injected, displacement gradually occurred on both sides of the rock, centered around the wellbore. Analysis presented in Section 3.2 confirmed that FPZ began to develop at t=20 s. It can be observed from Fig. 12 that before the development of the FPZ (t≤20 s), numerous discrete stress concentration points were distributed on the specimen surface. This phenomenon arises fundamentally due to the incoordination of rock deformation, which was caused by internal defects and heterogeneity. During the FPZ development stage (20 s≤t≤24 s), a large number of micro-cracks formed at the prefabricated crack tip, which led to stress release at these discrete stress concentration points. This process resulted in greater energy dissipation within the FPZ, and the FPZ exhibited a narrow band-like shape. During the fracture propagation stage (t>24 s), the fully developed FPZ dominated the fracture behaviour.

At t=24 s, the injection pressure reached its peak, and new fractures within the specimen initiated along the prefabricated cracks and propagated asymmetrically, as shown in Fig. 9c. In addition, the two fractures on the specimen surface merged near the wellbore wall to form a continuous fracture. The fracture propagation path in Fig. 9c occurred because the strength of the epoxy resin sealing the specimen's surface is significantly higher than that of the rock. This caused the internal cracks to slightly deviate at the epoxy resin-rock cementation interface as they propagated vertically toward the surface. Fig. 11 illustrates a mode I-II composite fracture, where the fracture on the left side propagated toward the boundary first.

3.4. Comparison of experimental and theoretical FPZ lengths

The validity of correlation equation was confirmed through a comparison of the DIC-measured FPZ lengths with their theoretically predicted value. It is important to clarify that in-situ stress enhances both the fracture toughness and tensile strength of the rock [44]. Brazilian tests conducted under 1 MPa confinement measured a tensile strength of 3.07 MPa, which demonstrated a 119% enhancement relative to unconfined conditions (1.4 MPa).

Rock heterogeneity can induce fracture deflection during propagation, which is potentially influenced by microstructural variations near the fracture tip or localized stress concentrations. As shown in Fig. 9b, the fracture deviated approximately 10° from the orientation of the maximum in-situ stress. Since the hydraulic fracture propagation criterion proposed in this study was derived from the assumption of mode I fracture, we only utilized the FPZ length monitored before the breakdown pressure for verification. The key fracture parameters before the breakdown pressure are summarized in Table 2. Fig. 13a shows the development process of FPZ over the injection duration, which confirmed that the theoretical predictions align closely with experimental measurements. Fig. 13b and c show the deformation area of the FPZ, which is consistent with mode I fracture behavior. Consequently, the correlation equation derived in Section 2 demonstrates a favorable reliability.

3.5. Apparent SIF and in-situ SIF

Fig. 14a shows the variations of apparent SIF and in-situ SIF over the injection duration. The stress intensity at the fracture

Table 2
Experimental and fracture parameters.

Duration (s)	Fluid pressure (MPa)	Experimental FPZ length (mm)	Theoretical FPZ length (mm)	Apparent SIF (MPa·mm$^{0.5}$)	In-situ SIF (MPa·mm$^{0.5}$)
20	2.19	2.17	1.87	6.65	4.47
21	2.44	2.79	2.75	8.06	5.41
22	2.69	3.41	3.78	9.46	6.36
23	2.93	4.96	4.95	10.82	7.27
24 (peak moment)	3.07	5.27	5.67	11.58	7.78

Note: Free fracture length is 10.00 mm.

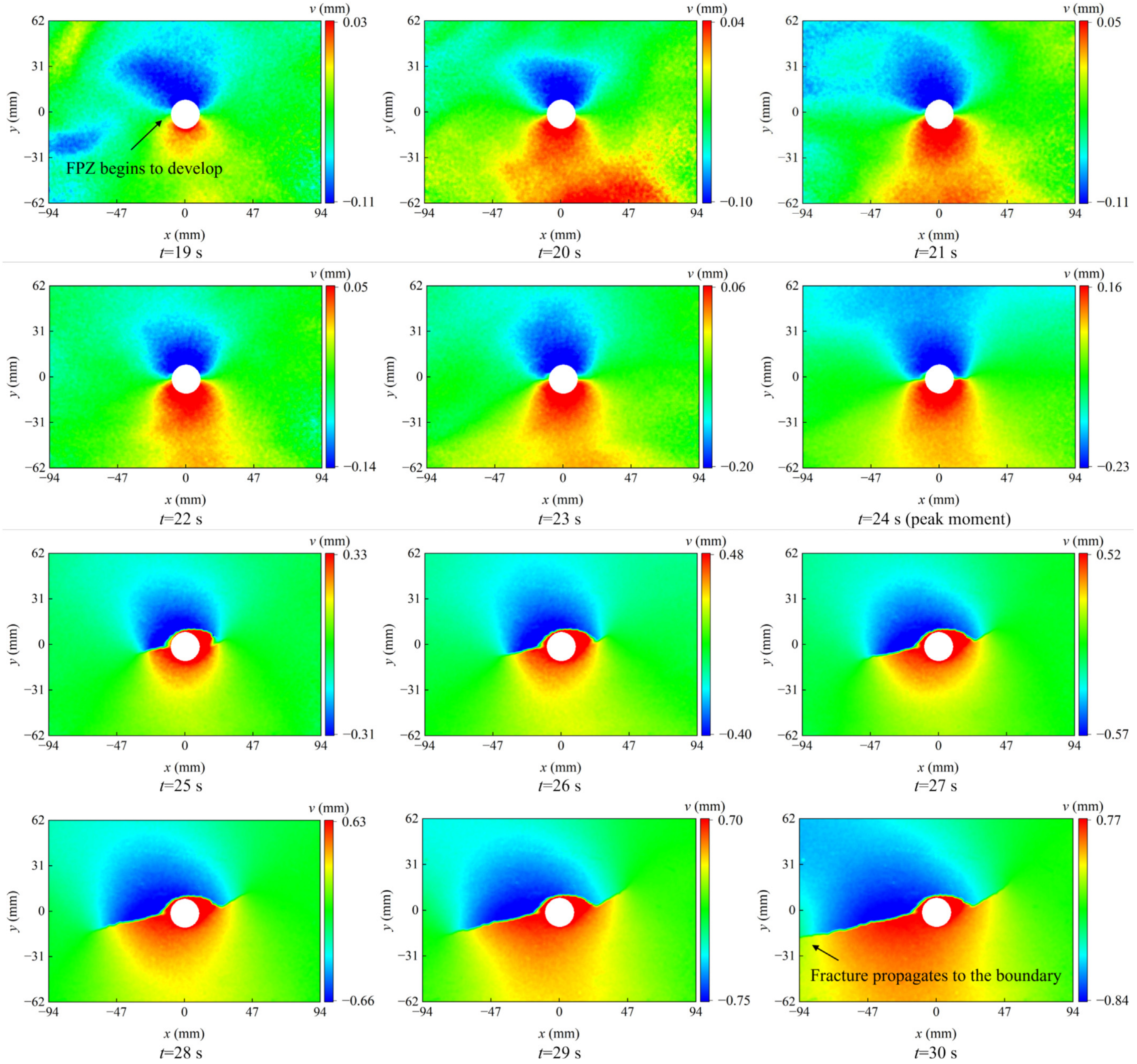

Fig. 11. Changes in the displacement field during the fracturing process.

tip increased with the injection pressure. At the peak moment, the stress intensity reached its maximum value, while the apparent fracture toughness was 11.58 MPa·mm$^{0.5}$, and the in-situ fracture toughness was 7.78 MPa·mm$^{0.5}$ (see Table 2). According to Eq. (22), the ratio of in-situ SIF to apparent SIF is determined by the minimum in-situ stress and tensile strength: $1-3\sigma_{\mathrm{h}}/(3\sigma_{\mathrm{h}}+2f_{\mathrm{t}})$. In this case where σ_{h}=1 MPa and f_{t}=3.07 MPa, the ratio of in-situ SIF/apparent SIF was determined to be 0.67, as depicted in Fig. 14b.

4. Verification of nonlinear hydraulic fracture propagation criterion

4.1. Verification scheme and experiments

This section presented the true triaxial hydraulic fracturing experiments and fracture experiments conducted under confining pressure. The reliability of the nonlinear hydraulic fracture propagation criterion was verified through the analysis of the FPZ's dynamic development and the comparison between experimental and predicted breakdown pressures. Two independent true triaxial hydraulic fracturing experiments were designed. The vertical in-situ stress and maximum horizontal in-situ stress were fixed at 30 and 28 MPa, respectively, while the minimum horizontal in-situ stress was set at 15 and 25 MPa, respectively, to obtain the actual breakdown pressures in the experiments. Following the criterion application process depicted in Fig. 7, three-point bending tests and Brazilian splitting tests were conducted under confining pressures of 15 and 25 MPa to obtain the fracture parameters. These parameters were then used to calculate the FFZ length and predict the breakdown pressure. It is worth noting that the above experimental specimens and visual fracturing specimens share to the same lithology, and their mechanical and physical parameters were described in Section 3.1.1.

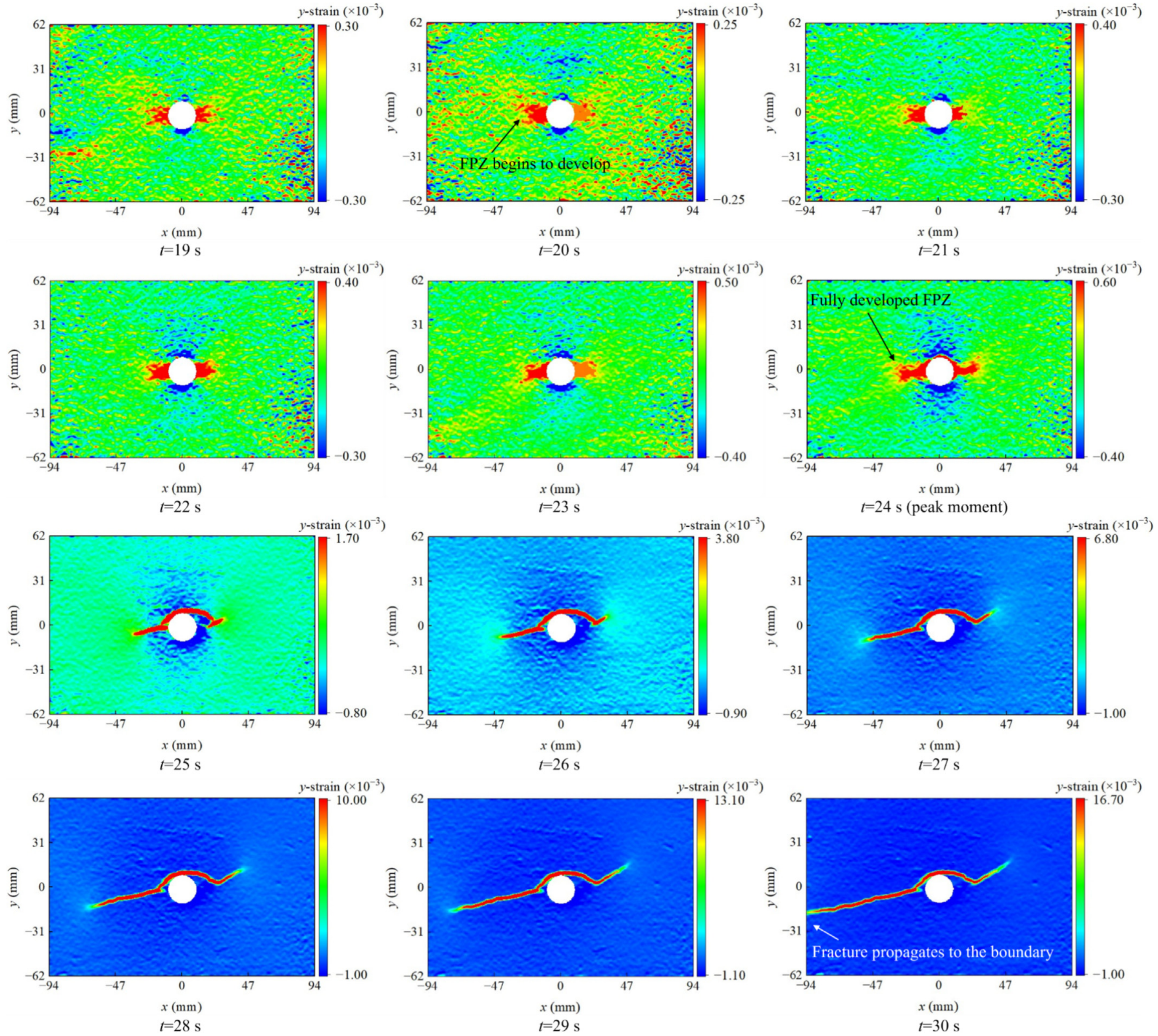

t=19 s
t=20 s
t=21 s
t=22 s
t=23 s
t=24 s (peak moment)
t=25 s
t=26 s
t=27 s
t=28 s
t=29 s
t=30 s

Fig. 12. Changes in the *y*-strain field during the fracturing process.

4.1.1. True triaxial hydraulic fracturing experiment

As depicted in Fig. 15a, the experiments were conducted using a large-scale true triaxial hydraulic fracturing test system independently developed by China University of Petroleum-Beijing. The test system comprises a large-size true triaxial test frame, a stress servo control system, a constant-speed and constant-pressure metering pump, an oil-water separator, a pressure monitor, a data acquisition system, and additional auxiliary devices. The experimental specimens were processed into standard cubic blocks measuring 300 mm × 300 mm × 300 mm. A vertical borehole with a depth of 150 mm and a diameter of 20 mm was drilled at the geometric center of the specimen. A 10 mm long prefabricated crack was created at the base of the wellbore to simulate the perforated section. An injection pipeline with a diameter of 3 mm was inserted into the vertical wellbore. A barefoot interval was installed at the bottom of the wellbore for fracturing, while the remaining section was sealed with epoxy resin adhesive. To ensure that new fractures initiate along the prefabricated crack, a horizontal minimum in-situ stress was applied perpendicular to the wellbore direction. To ensure that the in-situ stress applied to the surface of the specimens is fully transferred to the interior, thereby reducing experimental error, the specimens were pre-tightened for 2 h before fracturing, as recommended by Qiu [45]. The fracturing fluid mixture is consistent with that described in Section 3.1.2. The injection rate of fracturing fluid was maintained at 10 mL/min, with a viscosity of 300 cP.

As illustrated in Fig. 15b, the breakdown pressures were 30.95 and 49.35 MPa under the minimum in-situ stresses of 15 and 25 MPa, respectively. The fracture propagation pressures exceeded the minimum in-situ stress. This indicated that the in-situ stress applied to the specimen surface was fully transmitted to the interior, thus confirming the reliability of the experimental results.

4.1.2. Fracture experiment under confining pressure

As shown in Fig. 16, the experimental equipment used is an electro-hydraulic servo-controlled rock triaxial testing machine

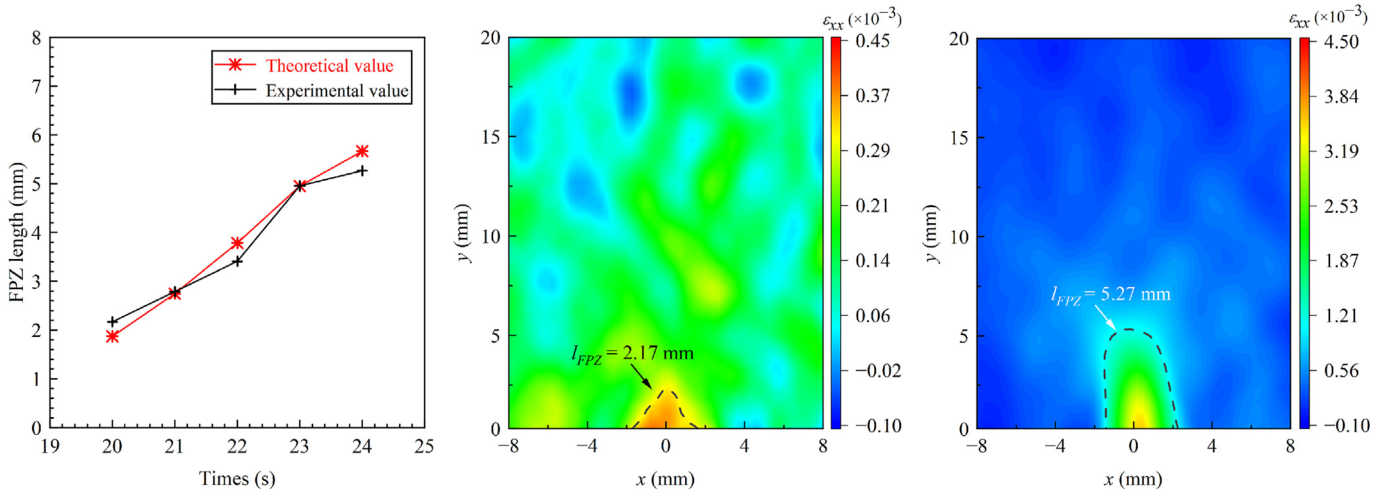

(a) FPZ length (b) t=20 s (c) t=24 s

Fig. 13. FPZ length and strain nephograms.

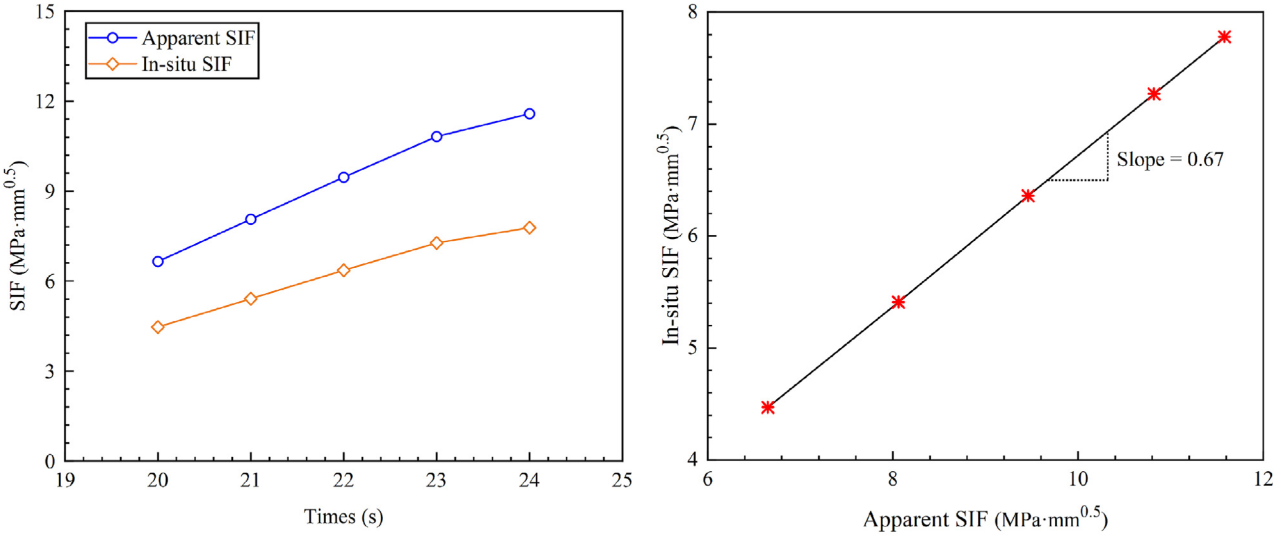

(a) Apparent SIF and in-situ SIF (b) The relationship between SIFs

Fig. 14. Variations of apparent SIF and in-situ SIF over the injection duration and their relationship.

developed by China University of Petroleum-Beijing, which features a stiffness greater than 1000 kN/mm. The experimental system consists of a confining pressure chamber, a three-point bending fixture, a Brazilian splitting fixture, a stress servo control system, a data acquisition system, and other auxiliary devices. The conventional fracture testing methodology was improved to obtain the apparent fracture toughness and tensile strength of rock under confining pressure. The specimen was tightly wrapped in a heat-shrinkable tube to isolate it from the liquid, as shown in Fig. 16a and b. In the three-point bending test conducted under confining pressure, the specimens were processed into standard single-ended notched beams (SENBs) with a length of 150 mm, a height of 50 mm, a thickness of 25 mm, and a span of 125 mm. Artificial fractures with a length of 15 mm and a width of 1 mm were prefabricated perpendicular to the bottom edge of the specimen using rock wire cutting technology. The specimen has a span-to-height ratio of 2.5 and a prefabricated crack length-to-height ratio of 0.3. Its dimensions meet international testing standards. The specimens utilized for the Brazilian split test under confining pressure were processed into standard cylinders with a diameter of 25 mm and a height of 12.5 mm. Displacement control was employed to load the specimens at a constant loading rate of 0.02 mm/min. For the experiment, confining pressure was applied first, and then axial load was applied until the specimen failed. It is worth noting that the heat-shrinkable tube was damaged upon the specimen's failure, resulting in seal failure and a small amount of hydraulic oil seeping into the specimen surface. As shown in Fig. 16c, the infiltration thickness was less than 2 mm, which is significantly less than the specimen thickness of 25 mm, and it did not substantially impact the statistical results.

As depicted in Fig. 17, the rock's tensile strength was measured at 1.4 MPa and the fracture toughness was recorded at 0.23 MPa·m$^{0.5}$ under 0 MPa confining pressure. At a confining pressure of 15 MPa, the rock's tensile strength increased by 12.6 times to 17.64 MPa, while the apparent fracture toughness increased by 14.9 times to 3.43 MPa·m$^{0.5}$. The in-situ fracture toughness was calculated to be 1.51 MPa·m$^{0.5}$ using Eq. (23). At a confining pressure of 25 MPa, the rock's tensile strength increased by 19.1 times

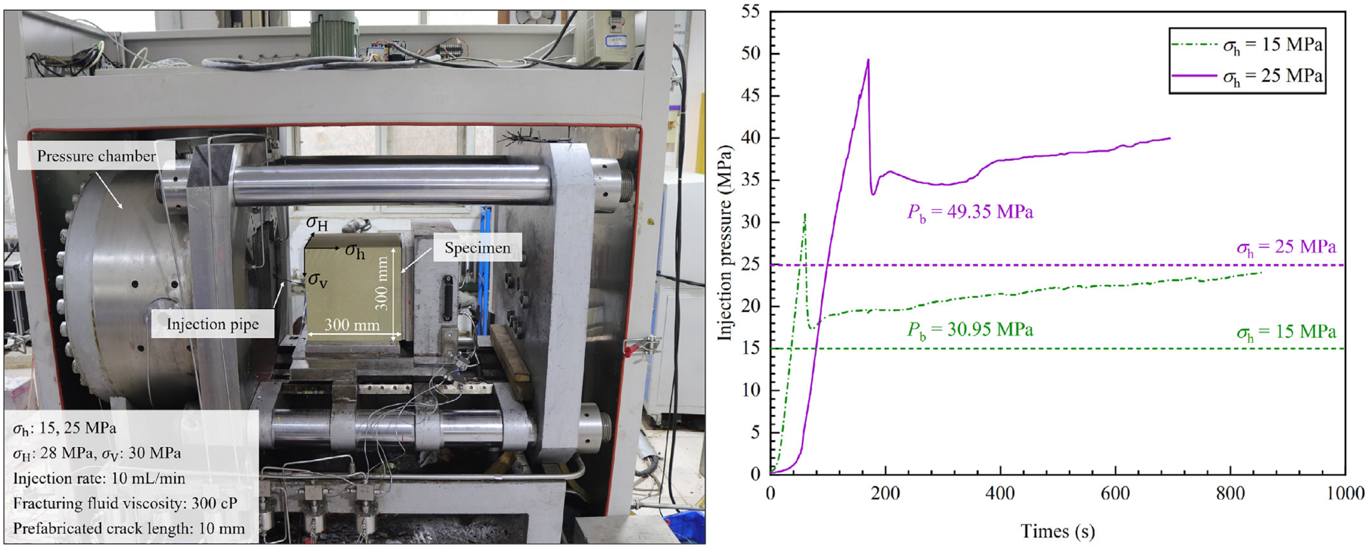

(a) Experimental device

(b) Injection curves

Fig. 15. True triaxial hydraulic fracturing experimental device and injection curves.

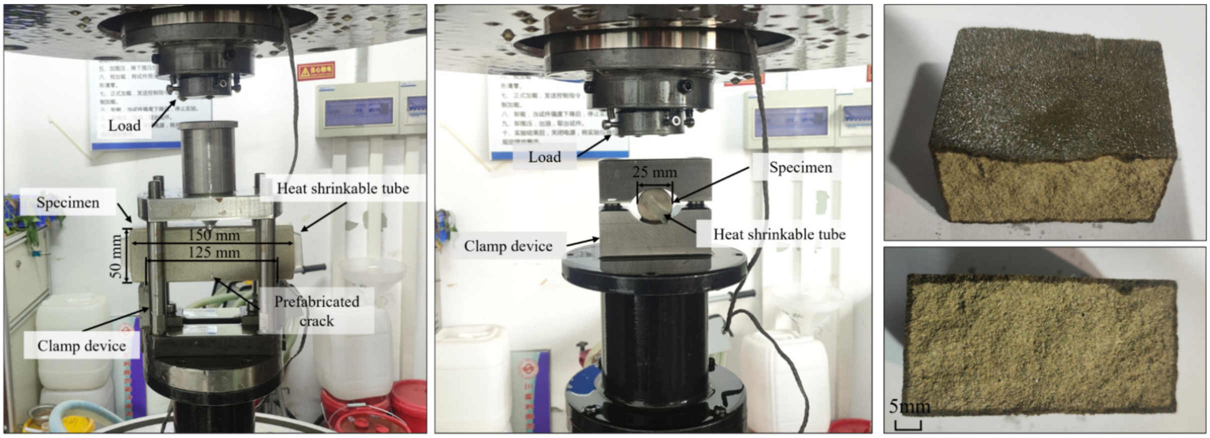

(a) Three-point bending test under confining pressure

(b) Brazilian test under confining pressure

(c) The specimen after experiment

Fig. 16. Fracture test under confining pressure.

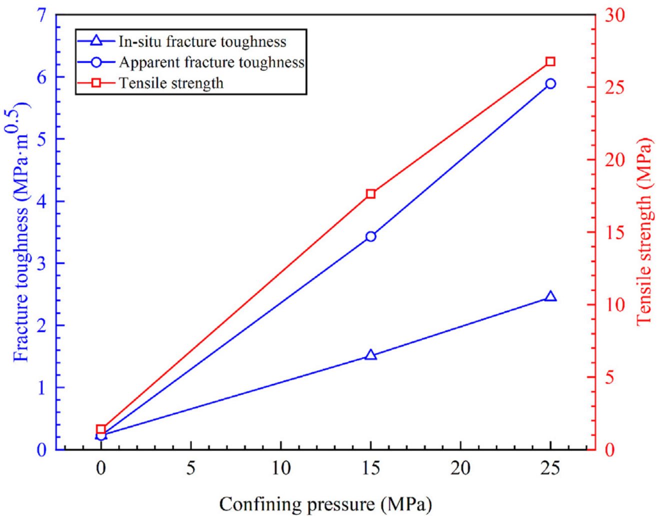

Fig. 17. Fracture parameters under confining pressure.

to 26.75 MPa, while the apparent fracture toughness increased by 25.6 times to 5.89 MPa·m$^{0.5}$, and the in-situ fracture toughness was 2.45 MPa·m$^{0.5}$. In summary, confining pressure has a strengthening effect on the fracture properties, while the fracture parameters increase linearly with increasing confining pressure.

4.2. Dynamic development law of the FPZ

To clarify the dynamic development behavior of the FPZ, the correlation equation is transformed as follows:

$$\frac{r_p}{a} = \frac{9\pi^2}{8}\left(\frac{\frac{P_f}{\sigma_h}-1}{3+2\frac{f_t}{\sigma_h}}\right)^2 \tag{35}$$

where r_p/a is the dimensionless FPZ length; and P_f/σ_h the dimensionless fluid pressure.

The fracture parameters obtained under confining pressure in Section 4.1.2, along with the fracturing curve data shown in Fig. 15b, were substituted into Eq. (35) to obtain the dynamic development of dimensionless FPZ. Fig. 18a and b show the development of dimensionless FPZ over time under different in-situ

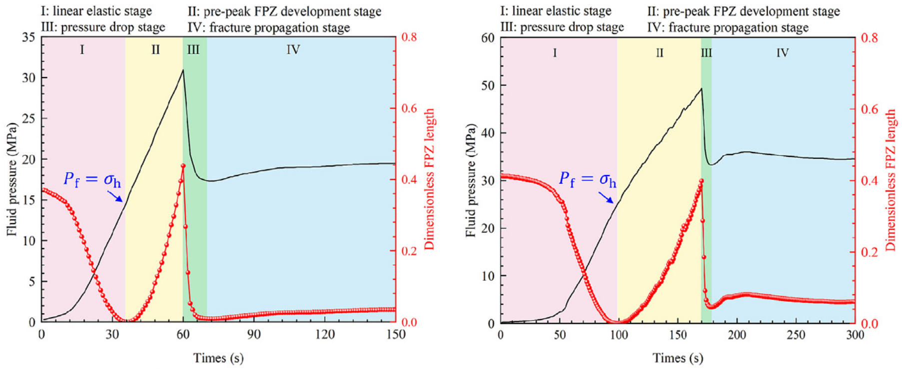

(a) σ_h = 15MPa (b) σ_h = 25MPa

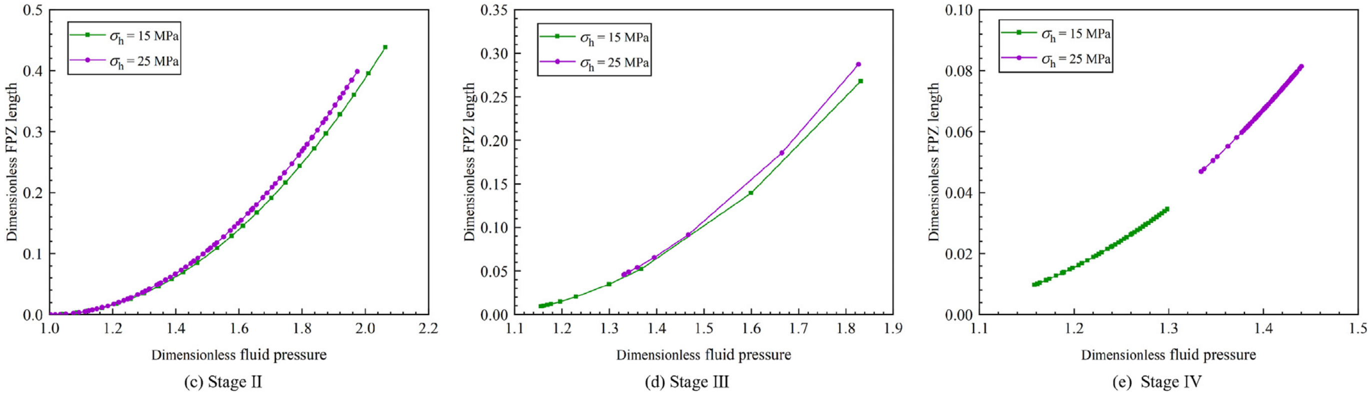

Fig. 18. Dynamic development of dimensionless FPZ.

stresses. According to the characteristics of the dimensionless FPZ curves, the dynamic development process of the FPZ is classified into four stages. Stage I: The specimen was in a state of linear elastic deformation, and the FPZ had not yet developed. During this stage, the calculated dimensionless FPZ length lacks physical significance. Stage II: When the fluid pressure exceeded the minimum in-situ stress, the FPZ began to develop, and the dimensionless FPZ length increased in a parabolic manner with the injection pressure and reached a maximum value at the peak moment. Stage III: Specimen failure led to drops in both fluid pressure and dimensionless FPZ length. Stage IV: Fracture propagation stabilized, and the dimensionless FPZ length followed the trend of the injection curve, exhibiting only minor variations during the propagation process. Fig. 18c–e showed that the dimensionless FPZ length exhibits a quadratic relationship with the dimensionless fluid pressure, with a slightly larger dimensionless FPZ length observed at higher in-situ stresses.

Prior to reaching breakdown pressure, the free fracture length remained equivalent to the initial prefabricated crack length of 10 mm. By substituting the fracture parameters obtained in Section 4.1.2 into Eqs. (26) or (27), the calculated FPZ lengths at peak stress were determine to be 4.38 and 3.98 mm for minimum horizontal in-situ stresses of 15 and 25 MPa, respectively. This finding indicates that greater in-situ stress correlates with a smaller FPZ size, which is consistent with the research results of Hashida et al. [46]. Increased in-situ stress suppressed microcracking within the FPZ, leading to a significant reduction in FPZ size. Consequently, a reduced FPZ requires a greater driving force to sustain further fracture propagation.

4.3. Prediction of breakdown pressures

The accuracy of the theoretical model was verified by analyzing the fracture path and breakdown pressure. Fig. 19a and b revealed that hydraulic fractures initiated along prefabricated cracks. The fracture mode was determined by the first derivative (dy/dx) of the fracture path curve. When $dy/dx \approx 0$, the fracture path curve forms a horizontal straight line parallel to the x-axis (σ_H direction), and the hydraulic fracture mode is classified as mode I fracture. Fig. 19c revealed that the length of mode I fractures near the wellbore was 77 mm under in-situ stress conditions of 15–28–30 MP, while Fig. 19d showed that the mode I fractures length near the wellbore was 48 mm under in-situ stress conditions of 25–28–30 MPa. These results demonstrated that the fractures near the wellbore are classified as mode I fracture when the fluid pressure reaches the breakdown pressure. This observation aligns with the mode I fracture assumption underlying the nonlinear hydraulic fracture propagation criterion proposed in this study. Therefore, the breakdown pressures obtained from the experiment exhibit comparability with the theoretical predictions.

A comparative analysis was conducted between the experimental data and theoretical values predicted by the nonlinear propagation criterion proposed in this study and the linear elastic fracture criterion. The key parameters for the linear elastic prediction are summarized in Table 3. Substituting the fracture parameters measured under confining pressure in Section 4.1.2 into Eq. (29) yielded the breakdown pressure predicted by the nonlinear propagation criterion. As illustrated in Fig. 20, the breakdown pressure predicted by the linear elastic propagation criterion is significantly lower than the experimental value. It approximates only half of the actual breakdown pressure, with a relative error of approximately 50%. In contrast, the fracture pressure predicted by the proposed nonlinear propagation criterion aligned closely with the experimental values. At a minimum in-situ stress of 15 MPa, the difference between predicted and actual values was merely 3.4 MPa (11.0% error), while at 25 MPa, the difference was 8.88 MPa (18% error). Overall, the breakdown pressure prediction method proposed in this study demonstrates a notable reliability.

The verification results of the FPZ length model in Section 3, the analysis of the dynamic development law of FPZ, and the verifica-

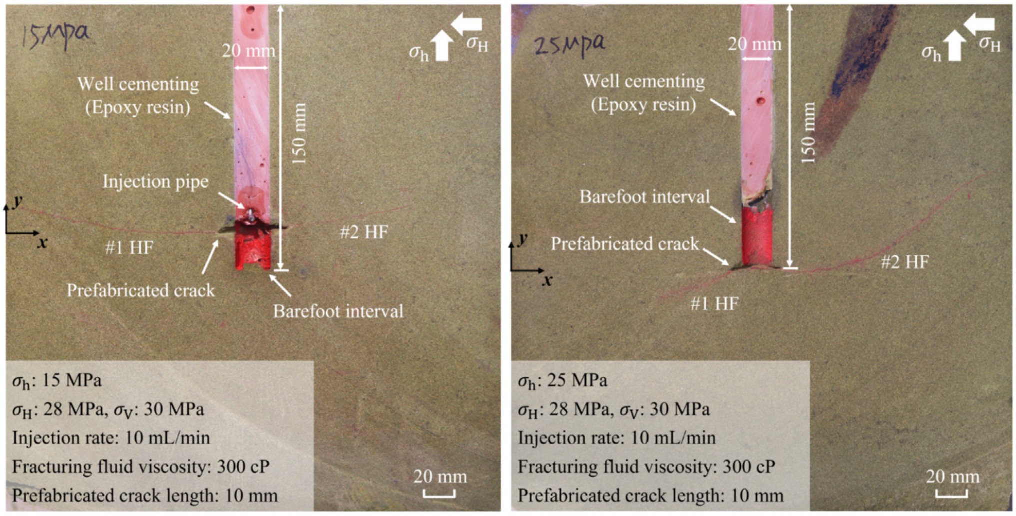

(a) Fracture morphology under σ_h = 15 MPa (b) Fracture morphology under σ_h = 25 MPa

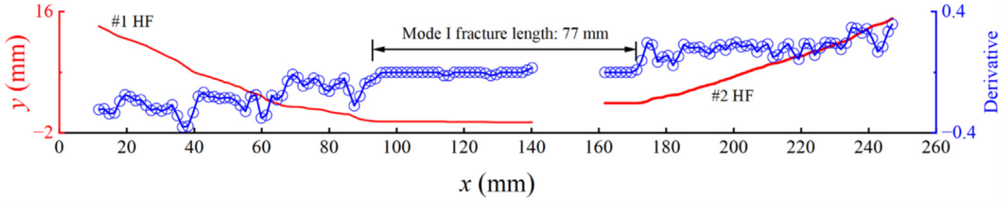

(c) First derivative of the fracture path curve under σ_h = 15 MPa

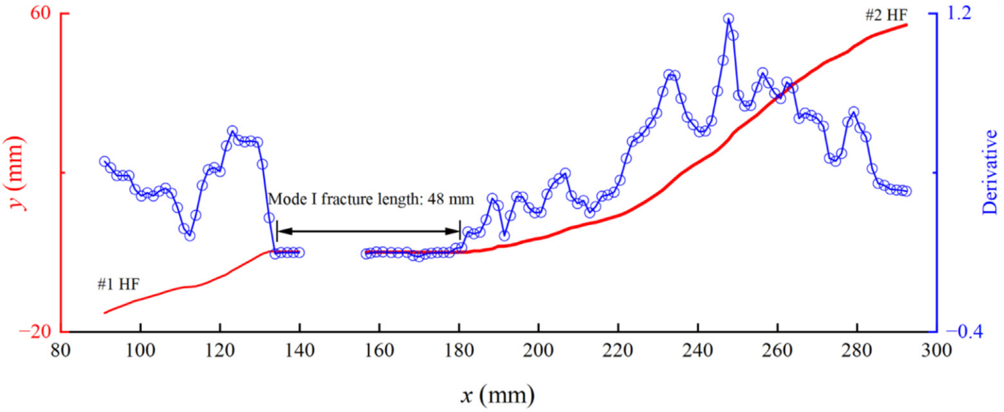

(d) First derivative of the fracture path curve under σ_h = 25 MPa

Fig. 19. Analysis of fracture morphology and path.

Table 3
Key parameters for predicting breakdown pressure using linear elastic method.

a (mm)	R_0 (mm)	K_{IC} (MPa·m$^{0.5}$)	b	h_0	h_a	$f(b)$	$g(b)$
10.0	10.0	0.23	2.0	0.729	1.671	−0.173	2.535

Note: The pressure gradient along the fracture is constant.

tion of the breakdown pressure in Section 4 collectively confirm that the nonlinear hydraulic fracture propagation criterion, which considers the fracture process zone, demonstrates high accuracy and reliability.

5. Discussion

5.1. Analysis of FPZ characteristics in reservoir

FPZ exhibits a significant size effect as its length is affected by the length of free fractures. It can be inferred that the length of the FPZ in actual reservoirs may range from sub-meter to meter scales. A most typical example is provided by Rector et al. [47], who analyzed the amplitude characteristics of cone waves generated during the fracturing process in the South Belridge Field in California. Their study revealed the existence of a fracture process zone measuring 27 m in length at the main fracture tip. Other researchers have also identified meter-sized FPZs through various seismic wave characteristics [48,49].

Mohammad et al. [48] conducted a comparative study of hydraulic fracture modeling and micro-seismic mapping results. As illustrated in Fig. 21, for wells D1 and S1, the average percentage

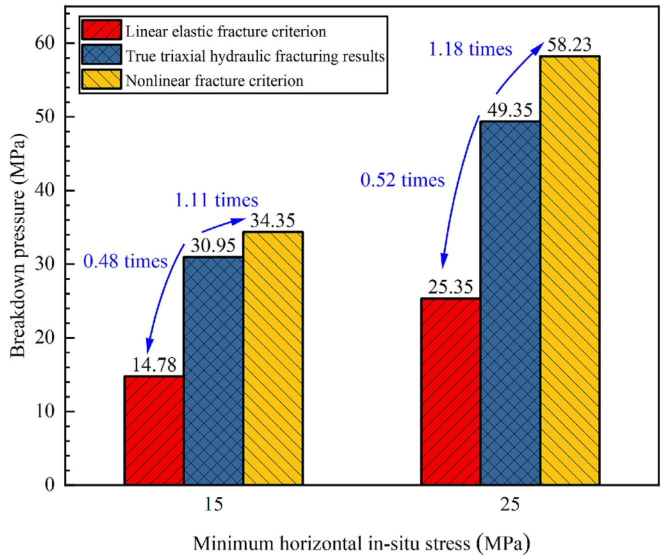

Fig. 20. Comparison of breakdown pressures predicted by different fracture propagation criteria.

differences in the total hydraulic fracture length between the fracture modeling and micro-seismic mapping were 34.07% and 31.73%, respectively. Notably, the hydraulic fracture lengths obtained from micro-seismic mapping were longer than those predicted by fracture modeling. This observation suggests that micro-seismic events may originate not directly along the hydraulic fracture but rather at some offset distance, either laterally or ahead of the fracture front. According to Warpinski et al. [49], who studied B-Sand at Site M in the Piceance Basin of Colorado, micro-seismic events can occur 3.7 to 4.6 m in front of the fracture tip and 4.6 to 6.1 m perpendicular to the fracture tip due to the high stress concentration at the fracture tip. These findings further confirm the existence of meter-scale nonlinear FPZs at the hydraulic fracture tip during field fracturing activities.

The aforementioned field fracturing cases further revealed that the inverted fracture length obtained through microseismic monitoring in deep reservoirs was often greater than the actual fracture length. This discrepancy arose from the inability to effectively distinguish between the macro-fracture and the FPZ during microseismic data analysis, which led to an overestimation of fracture length. Specifically, when these two types of vibration signals cannot be clearly differentiated during analysis, small vibrations originating from the FPZ are often mistakenly attributed to the macro-fracture propagation, which results in an overestimation of the fracture scale. Therefore, accurately distinguishing between the macro-fracture and the FPZ is crucial for assessing the actual scale of the fracture. Achieving this requires the introduction of more geological and physical models into the data analysis process and the combination of multiple monitoring methods to improve the accuracy of fracture scale estimation.

5.2. Potential field application

In deep reservoirs, there is a nonlinear fracture process zone at the hydraulic fracture tip. When designing the hydraulic fracturing process, it is necessary to accurately evaluate the reservoir breakdown pressure and the FPZ size. The proposed breakdown pressure prediction method considering FPZ enables accurate pre-fracturing evaluations through the analysis of key parameters, including apparent or in-situ fracture toughness, tensile strength, and in-situ stress. This approach ultimately enhances the effectiveness of reservoir stimulation. As illustrated in Fig. 22, a stress unloading damage band formed near the main fracture after the unloading of the FPZ [36]. Once the fracturing fluid was lost into the micro-fractures, branch fractures were generated. Stimulating the micro-fracture network in the damaged band to form a complex fracture network is essential for increasing the stimulation volume.

5.3. The challenges of nonlinear propagation criteria from 2D to 3D

The nonlinear hydraulic fracture propagation criterion proposed in this study is based on two-dimensional plane analysis. While it effectively predicts the breakdown pressure and the length of the FPZ, it is unable to fully describe three-dimensional fracture propagation behavior. The actual hydraulic fracture in reservoirs exhibits complex, three-dimensional geometries, which poses significant challenges in extending nonlinear hydraulic fracture propagation criteria from two-dimensional to three-

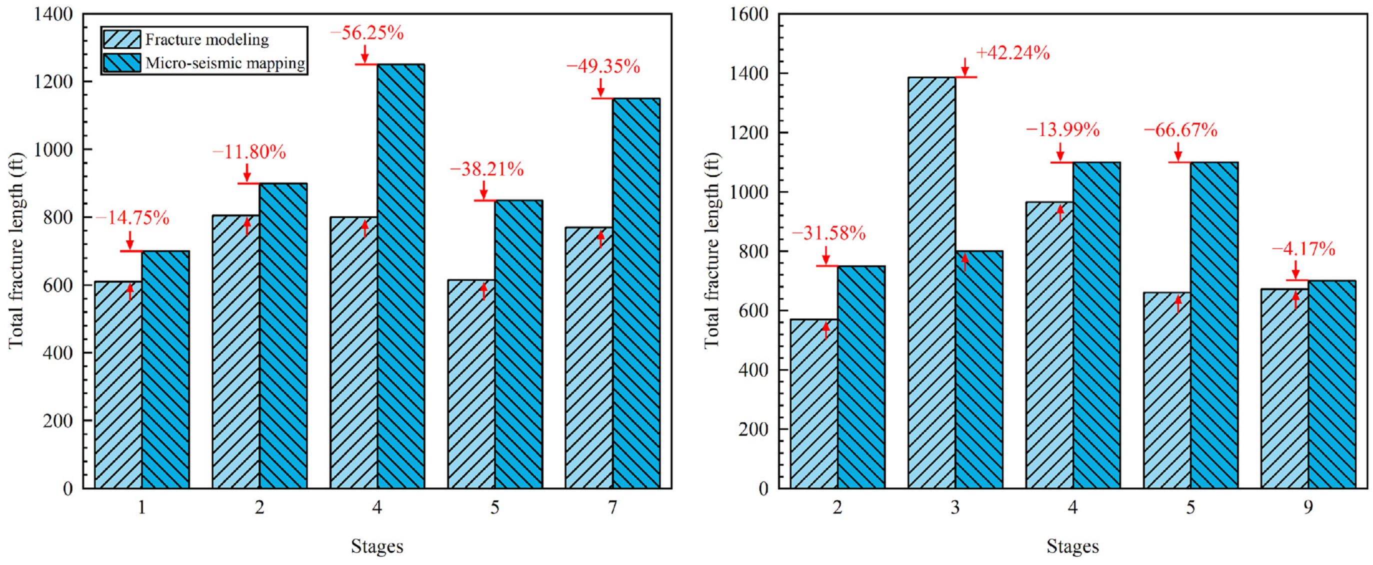

(a) Well-D1
(b) Well-S1

Fig. 21. Comparison of fracture lengths derived from fracture modeling and micro-seismic mapping for two wells in the Greater Natural Buttes field, Unita Basin, Utah [48].

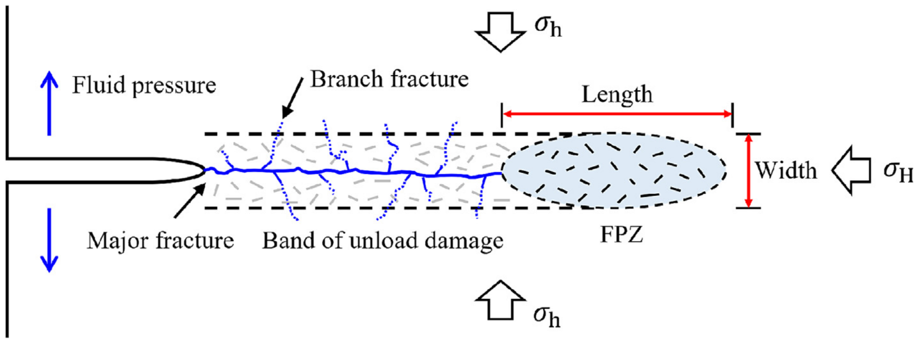

Fig. 22. Schematic diagram of the FPZ at the fracture tip and the damage band.

dimensional analysis. These challenges are fundamental and can be summarized as follows:

(1) Three-dimensional hydraulic fractures exhibit more complex geometric shapes. The leading fracture front is no longer a point but a spatial curve. Describing the shape, orientation, and temporal evolution of this fracture poses a considerable challenge.
(2) The direction of three-dimensional hydraulic fracture propagation is difficult to predict due to its dependence on the local three-dimensional stress field and the inherent heterogeneity of the rock.
(3) The stress intensity factor varies along the fracture front, which makes the definition of a three-dimensional fracture criterion to govern the propagation of the entire fracture front particularly difficult. Furthermore, accurately characterizing the three-dimensional morphology of the nonlinear zone remains a significant challenge.
(4) The distribution of fluid pressure within the fracture is uneven across its height, length, and width, and is influenced by the local fracture opening. The fluid within three-dimensional hydraulic fractures no longer flows in a single direction but instead requires solving complex three-dimensional fluid dynamics equations. Despite these challenges, developing reliable three-dimensional nonlinear hydraulic fracture propagation criteria is critical for advancing oil and gas extraction technologies.

6. Conclusions

In this study, we profiled the closing stress acting on the FPZ by superposing the in-situ stress onto the cohesive stress and then developed a new fracture criterion for nonlinear fracture. By assuming zero stress intensity at the fracture tip, we derived three key parameters: apparent fracture toughness, in-situ fracture toughness, FPZ length. Additionally, the correlation between breakdown pressure and FPZ length was developed, and a nonlinear hydraulic fracture propagation criterion considering FPZ was established. The reliability of the criterion was validated through a visualized hydraulic fracturing experiment and a true triaxial hydraulic fracturing experiment. The main conclusions are as follows:

(1) The length model of the FPZ derived in this study can accurately describe the developing process and mechanical behavior of the nonlinear FPZ at the hydraulic fracture tip. For a specific reservoir, the FPZ length is predominantly influenced by fluid pressure and fracture length, and it has a quadratic relationship with the injection fluid pressure.
(2) The FPZ began to develop when fluid pressure exceeded the minimum in-situ stress. The dimensionless FPZ length exhibited parabolic growth with increasing fluid pressure and reached its maximum value at the peak moment.
(3) In-situ fracture toughness and apparent fracture toughness serve as critical parameters for assessing fracture propagation. Their ratio follows the expression $1-3\sigma_{\mathrm{h}}/(3\sigma_{\mathrm{h}}+2f_{\mathrm{t}})$, where confining pressure demonstrates a positive linear correlation with both toughness parameters.
(4) The proposed nonlinear hydraulic fracture propagation criterion can effectively describe the FPZ length at the fracture tip, accurately predict the breakdown pressure during fracturing operations, and establish a relationship between these two parameters. It addresses the inherent limitations of conventional LEFM, which often underestimates fracture toughness and neglects the effects of the FPZ.

Acknowledgement

This work was supported by the National Natural Science Foundation of China (No. 52434001).

References

[1] Luo P, Luo WG, Li S. Effectiveness of miscible and immiscible gas flooding in recovering tight oil from Bakken reservoirs in Saskatchewan, Canada. Fuel 2017;208:626–36.
[2] Solarin SA, Gil-Alana LA, Lafuente C. An investigation of long range reliance on shale oil and shale gas production in the U.S. market. Energy 2020;195:116933.
[3] Zheng M, Li JZ, Wu XZ, Li P, Wang WG, Wang SJ, Xie HB. Physical modeling of oil charging in tight reservoirs: A case study of Permian Lucaogou Formation in Jimsar Sag, Junggar Basin, NW China. Petrol Explor Dev 2016;43(2):241–50.
[4] Zhou ZL, Hou ZK, Guo YT, Zhao H, Wang D, Qiu GZ, Guo WH. Experimental study of hydraulic fracturing for deep shale reservoir. Eng Fract Mech 2024;307:110259.
[5] Zhou CB, Ye ZY, Yao C, Fan XC, Xiong F. Estimation of the anisotropy of hydraulic conductivity through 3D fracture networks using the directional geological entropy. Int J Min Sci Technol 2024;34(2):137–48.
[6] Zhou Q, Zhu ZM, Liu W, Lu HJ, Fan ZD, Nie XF, Li CB, Wang J, Ren L. Hydraulic fracturing behaviors of shale under coupled stress and temperature conditions simulating different burial depths. Int J Min Sci Technol 2024;34(6):783–97.
[7] Zhang X, Jeffrey RG, Bunger AP, Thiercelin M. Initiation and growth of a hydraulic fracture from a circular wellbore. Int J Rock Mech Min Sci 2011;48(6):984–95.
[8] Garagash DI. Cohesive-zone effects in hydraulic fracture propagation. J Mech Phys Solids 2019;133:103727.
[9] Yue KM, Lee HP, Olson JE, Schultz RA. Apparent fracture toughness for LEFM applications in hydraulic fracture modeling. Eng Fract Mech 2020;230:106984.
[10] Zhu DW, Han GF, Zou HL, Cui MY, Liang C, Yao F. A review of the hydraulic fracturing in ductile reservoirs: Theory, simulation, and experiment. Processes 2022;10(10):2022.
[11] Barenblatt GI. The mathematical theory of equilibrium cracks in brittle fracture. Adv Appl Mech 1962;7:55–129.
[12] Papanastasiou P, Thiercelin M. Influence of inelastic rock behaviour in hydraulic fracturing. Int J Rock Mech Min Sci Geomech Abstr 1993;30(7):1241–7.

[13] Pan R, Zhang GQ, Li SY, Zheng XL, Xu CZ, Fan ZY. Influence of the fracture process zone on fracture propagation mode in layered rocks. J Petrol Sci Eng 2021;202:108524.

[14] Sun FQ, Du SH, Zhao YP. Fluctuation of fracturing curves indicates in-situ brittleness and reservoir fracturing characteristics in unconventional energy exploitation. Energy 2022;252:124043.

[15] Sun Z, Zhao YX, Gao YR, Elmo D, Gao S, Wang XL. Effect of size and anisotropy on fracture process zone of coal: An experiment and numerical simulation. Eng Fract Mech 2024;306:110227.

[16] Zhuang DD, Yin TB, Li Q, Wu Y, Chen YJ, Yang Z. Fractal fracture toughness measurements of heat-treated granite using hydraulic fracturing under different injection flow rates. Theor Appl Fract Mech 2022;119:103340.

[17] Gehne S, Forbes Inskip ND, Benson PM, Meredith PG, Koor N. Fluid-driven tensile fracture and fracture toughness in Nash Point shale at elevated pressure. J Geophys Res Solid Earth 2020;125(2):e2019JB018971.

[18] Rubin AM. Tensile fracture of rock at high confining pressure: Implications for dike propagation. J Geophys Res Solid Earth 1993;98(B9):15919–35.

[19] Luo SL, Zhang GQ, Sun B, Qiu RY, Ling YS. Numerical study on mode I fracture characteristics of rock under confining pressure. In: Proceedings of the 58th U. S. Rock Mechanics/Geomechanics Symposium. Colorado: ARMA; 2024:ARMA-2024-0349.

[20] Guo H, Aziz NI, Schmidt LC. Rock fracture-toughness determination by the Brazilian test. Eng Geol 1993;33(3):177–88.

[21] Schmidt RA, Huddle CW. Effect of confining pressure on fracture toughness of Indiana limestone. Int J Rock Mech Min Sci Geomech Abstr 1977;14(5–6):289–93.

[22] Al-Shayea NA, Khan K, Abduljauwad SN. Effects of confining pressure and temperature on mixed-mode (I-II) fracture toughness of a limestone rock. Int J Rock Mech Min Sci 2000;37(4):629–43.

[23] Savitski AA, Detournay E. Propagation of a penny-shaped fluid-driven fracture in an impermeable rock: Asymptotic solutions. Int J Solids Struct 2002;39(26):6311–37.

[24] Abé H, Mura T, Keer LM. Growth rate of a penny-shaped crack in hydraulic fracturing of rocks. J Geophys Res 1976;81(29):5335–40.

[25] Scholz CH. A note on the scaling relations for opening mode fractures in rock. J Struct Geol 2010;32(10):1485–7.

[26] Zhao XL, Roegiers JC. Determination of in situ fracture toughness. Int J Rock Mech Min Sci Geomech Abstr 1993;30(7):837–40.

[27] Schmidt RA. A microcrack model and its significance to hydraulic fracturing and fracture toughness testing. In: Proceedings of the 21st U.S. Symposium on Rock Mechanics (USRMS). Missouri: American Rock Mechanics Association; 1980:ARMA-80-0581.

[28] Sato K, Hashida T. Cohesive crack analysis of toughness increase due to confining pressure. Pure Appl Geophys 2006;163(5):1059–72.

[29] Mokryakov V. Analytical solution for propagation of hydraulic fracture with Barenblatt's cohesive tip zone. Int J Fract 2011;169(2):159–68.

[30] Mejía Camones LA, do A Vargas Jr E, Velloso RQ, Paulino GH. Simulation of hydraulic fracturing processes in rocks by coupling the lattice Boltzmann model and the Park-Paulino-Roesler potential-based cohesive zone model. Int J Rock Mech Min Sci 2018;112:339–53.

[31] Yao Y. Linear elastic and cohesive fracture analysis to model hydraulic fracture in brittle and ductile rocks. Rock Mech Rock Eng 2012;45(3):375–87.

[32] Dugdale DS. Yielding of steel sheets containing slits. J Mech Phys Solids 1960;8(2):100–4.

[33] Barenblatt GI. The formation of equilibrium cracks during brittle fracture. General ideas and hypotheses. Axially-symmetric cracks. J Appl Math Mech 1959;23(3):622–36.

[34] Anderson TL, Anderson TL. Fracture mechanics: Fundamentals and applications. 3rd ed. Boca Raton: CRC Press; 2005.

[35] Tada H, Paris PC, Irwin GR. The stress analysis of cracks handbook. 3rd ed. New York: ASME Press; 2000.

[36] Bažant ZP, Le JL, Salviato M. Quasibrittle fracture mechanics and size effect: A first course. Oxford: Oxford University Press; 2021.

[37] Blaber J, Adair B, Antoniou A. Ncorr: Open-source 2D digital image correlation Matlab software. Exp Mech 2015;55(6):1105–22.

[38] Chen L, Zhang GQ, Zou ZK, Guo YZ, Zheng XL. The effect of fracture growth rate on fracture process zone development in quasi-brittle rock. Eng Fract Mech 2021;258:108086.

[39] Fatahi H, Hossain MM, Fallahzadeh SH, Mostofi M. Numerical simulation for the determination of hydraulic fracture initiation and breakdown pressure using distinct element method. J Nat Gas Sci Eng 2016;33:1219–32.

[40] Wu FP, Li D, Fan XZ, Liu J, Li XJ. Analytical interpretation of hydraulic fracturing initiation pressure and breakdown pressure. J Nat Gas Sci Eng 2020;76:103185.

[41] Lin Q, Labuz JF. Fracture of sandstone characterized by digital image correlation. Int J Rock Mech Min Sci 2013;60:235–45.

[42] Lin Q, Wang SQ, Pan PZ, Bian X, Lu YH. Imaging opening-mode fracture in sandstone under three-point bending: A direct identification of the fracture process zone and traction-free crack based on cohesive zone model. Int J Rock Mech Min Sci 2020;136:104516.

[43] Tang YX, Su RKL, Chen HN. Characterization on tensile behaviors of fracture process zone of nuclear graphite using a hybrid numerical and experimental approach. Carbon 2019;155:531–44.

[44] Li JZ, Zhang G, Liu MZ. Experimental investigation on the effect of confining pressure on the tensile strength of sandstone using hollow cylinder tensile test method. Arab J Geosci 2019;12(24):768.

[45] Qiu RY, Zhang GQ, Zheng XL, Luo SL, Chen HZ, Zhao JL. Stress transfer law in laboratory hydraulic fracturing experiments. Sci Rep 2024;14(1):17287.

[46] Hashida T, Oghikubo H, Takahashi H, Shoji T. Numerical simulation with experimental verification of the fracture behavior in granite under confining pressures based on the tension-softening model. Int J Fract 1993;59(1):227–44.

[47] Rector JW, Dong QC, Patzek TW. Passive characterization of hydrofracture properties using signals from hydraulic pumps. J Petrol Sci Eng 2000;27(1–2):49–58.

[48] Mohammad NA, Miskimins JL. A comparison of hydraulic fracture modeling with downhole and surface microseismic data in a stacked fluvial pay system. SPE Prod & Oper 2012;27(03):253–64.

[49] Warpinski NR, Wright TB, Uhl JE, Engler BP, Drozda PM, Peterson RE, Branagan PT. Microseismic monitoring of the B-sand hydraulic-fracture experiment at the DOE/GRI multisite project. SPE J 1999;4(3):242–50.